Controlling SALD-Deposited ZTO Nanofilm Composition and Implications for their use as Perovskite Solar Cell Transport Layers

by

Louis-Vincent Delumeau

A thesis
presented to the University of Waterloo
in fulfilment of the
thesis requirement for the degree of
Master of Applied Science
in
Mechanical and Mechatronics Engineering (Nanotechnology)

Waterloo, Ontario, Canada, 2021

AUTHOR'S DECLARATION

I hereby declare that I am the sole author of this thesis. This is a true copy of the thesis, including any required final revisions, as accepted by my examiners.

I understand that my thesis may be made electronically available to the public.

Abstract

This thesis is concerned with the study of new nanofilm electron transport layers for use in perovskite solar cells, one of the thin film solar cell technologies in the research and very early commercial phases. Spatial atomic layer deposition (SALD) is a method of nanofilm growth that is particularly well-suited to metal oxide fabrication, yielding high-quality uniform films in less time and without the cumbersome vacuum requirements of conventional atomic layer deposition. An important attribute of a performant electron transport layer is the appropriate matching of its conduction and valence band energy levels to those of the perovskite in contact with it, to favour electron extraction into the transport layer and prevent the entry of holes. Different absorber layers, with lead halide perovskites as only one example, will exhibit different energy levels; thus being able to tune the bandgap of the transport layer to better match the specific perovskite or other light absorber layer in use is very useful to be able to optimise a variety of solar cell designs for commercialisation. This was investigated in the context of zinc-tin oxide, a mixture of two of the most praised metal oxide electron transport layers for perovskite cells - ZnO and SnO_2.

The hope was that the bandgap of zinc-tin oxide, as deposited by SALD using an ozone-oxygen mixture, would vary with the Sn content (or Sn atom concentration relative to total metal atom concentration). Zinc-tin oxide was grown for the first time with SALD using different reactor head slits for each of the precursors - TDMASn and DEZ. For the oxide produced using the deposition conditions and compositions from this study, there is doubt as to whether a clear bandgap correlation with film composition was found, yet the results do point to other deposition conditions or post-deposition heat treatments that are likeliest to allow bandgap engineering, if such a relationship is valid for zinc-tin oxide. A wider range of zinc-tin oxide compositions by SALD was reported in this study than ever before (28% to 97% Sn content), and a detailed theory

explaining the relationship between the deposition conditions and Sn content of the films is put forward, suggesting Sn and Zn precursor flow rates to be selected according to the desired film composition. Nor was a clear trend with composition identified for as-deposited films for transmittance, refractive index, defect and majority carrier densities, or film morphology. Photoluminescence quenching to compare the electron extraction efficiencies of different oxide compositions pointed to an Sn content of 97% being least effective. Atomic layer depositions straight onto perovskite are confirmed to be completely incompatible with the use of ozone as the oxidiser.

Acknowledgements

A heartfelt thanks to Joseph Jessy and Nina Heinig of the UWaterloo WATLab for their assistance and expertise in X-ray analysis, and to Fan Ye who always lent a helping hand with his microscopy competence.

The same goes to Abdullah Alshehri and Hatameh Asgarimoghaddam for their tricks of the trade, which played a major role in speeding up the project.

So many films could not have been deposited without Alex Jones, who kept the deposition system in fighting condition - this thesis would not have been as complete without him.

A greater thanks still to Jhi Yong Loke and Chee Hau Teoh, for introducing me to the potential of ellipsometry, designing gradient reactor heads, and whose success I am not nearly done hearing about.

But most of all, to Kevin Musselman, without whose unwavering support and illuminating insight this thesis would have been completely blank.

Dedication

美矢へ

Table of Contents

List of Figures

List of Tables

List of Abbreviations

AFM	Atomic Force Microscope
CB	Conduction Band
DEZ	Diethylzinc
DLCP	Drive-Level Capacitance Profiling
DMA	Dimethylamino
EDX	Energy-Dispersive X-Ray Spectroscopy
E_g	Bandgap
ETL	Electron Transport Layer
FA^+	Formamidinium Ion
FF	Fill Factor
FTO	F-Doped Tin Oxide
GIXRD	Grazing Incidence X-Ray Diffraction
GPC	Growth Per Cycle
HTL	Hole Transport Layer
ITO	In-Doped Tin Oxide
J_{SC}	Short-Circuit Current
MA^+	Methylammonium Ion
MFC	Mass Flow Controller
PCE	Power Conversion Efficiency
PL	Photoluminescence
PSC	Perovskite Solar Cell
PTFE	Polytetrafluoroethylene
PV	Photovoltaic
(S)ALD	(Spatial) Atomic Layer Deposition
(S)CVD	(Spatial) Chemical Vapour Deposition
SEM	Scanning Electron Microscope

TCO	Transparent Conductive Oxide
TCSPC	Time-Correlated Single Photon Counting
TDMASn	Tetrakis(dimethylamino)tin(IV)
TL	Transport Layer
VB	Valence Band
V_{OC}	Open-Circuit Voltage
XPS	X-Ray Photoelectron Spectroscopy
ZTO	Zinc-Tin Oxide

CHAPTER 1: INTRODUCTION

1.1 Objectives of the Project

Perovskite solar cells (PSCs) may be the most promising thin film photovoltaic technology, in terms of their efficiency as well as ease of production, which can be done at much lower temperatures than are required to make traditional silicon-based solar cells. For these reasons, some experts believe they could replace silicon and become a mainstream photovoltaic technology, however a few major problems remain in their way. One is that their efficiencies are not yet high enough to justify replacing silicon cells with PSCs, at least not in the case of PSC designs that are appropriate for mass production. A second is scalability: too many steps in their production remain too slow for their commercial debut. Finally and perhaps most significantly is the fact that the stability of several of the layers in a PSC fall short of what is required in the development of a product with a service life superior to a few months. This includes the perovskite material itself, but some common polymer-based charge transport materials also face severe degradation problems. This project could play a role in the solving of all three of these problems, and help to bring PSCs significantly closer to the market, through the development of more performant electron transport layers (ETLs).

The principal motivation for this project was the idea that a well-chosen ETL material grown with a mass production-compatible nanofilm deposition technique that deposits uniform layers with a low defect concentration would be very beneficial to PSC development. The original objective was to grow SnO_2 as an ETL, a transparent conductive oxide (TCO) with high conductivity, electron mobility, density and stability, and a more appropriate bandgap than most other materials used as ETLs in PSCs of the n-i-p architecture (in which the ETL is the layer with the transparency

requirement). The project then shifted its focus to zinc-tin oxide (ZTO) as an ETL, a mixture of ZnO and SnO_2, which may be even more promising than these two already preferred ETL candidate TCOs thanks to the enhancement of electrical properties brought about by oxide doping, as well as a potential ability to tune the bandgap as a function of composition (though this still requires investigation), which may make ZTO compatible with a broad variety of perovskite materials. Not only could these tin-based TCOs be very performing as ETLs, but the method by which they were deposited brings about major advantages in quality over many other film-forming methods.

The objectives of the project were to characterise and document the morphological, optical and electrical properties of ZTO as a function of composition, in an effort to provide crucial information for PSC designers who may choose the promising ZTO candidate as an ETL material. Spatial atomic layer deposition (SALD) is a nanofilm deposition technique that produces very homogeneous layers with a low concentration of pin-hole defects. It is very appropriate for the production of metal oxides, and is a cost-effective method that does not have vacuum, high temperature, or other highly energy-demanding requirements. On top of this, it is relatively quick at depositing oxides, making the method scalable in that it is adaptable to a mass-production setting. With the investigation into ZTO deposition conditions completed, the hope was that a case would have been made for a very performant ETL that could bring photovoltaic efficiency improvements over other ETL materials for a wide range of absorber materials. This is because the bandgap of ZTO was suspected to change with its composition, allowing for the perfect composition to be chosen to maximise electrical performance. This can make ZTO the best ETL for a broad range of perovskites, or even a great TCO choice for non-PSC applications. The material would be compatible with industrial production, demonstrating that SALD should be chosen over methods

plagued by poorer control (such as spin-coating) wherever possible, if the end goal is to bring PSCs to the market.

1.2 Introduction to Photovoltaics

The purpose of a photovoltaic (PV) device or solar cell is to convert energy from a light source, usually the Sun, into useful electrical current to power a device or be stored in a battery. All solar cells must have a light absorbing material - the absorber layer - which absorbs incoming photons with sufficient energy by means of excitation of an electron to a higher energy level. Most often, electrons will be excited from the valence band (VB) of the absorber material to the conduction band (CB), leaving behind a hole. Electrons therefore go from the bonding state and are excited to an anti-bonding state by this process. Electrons excited into the CB and the positively charged holes they leave behind in the VB are both mobile and free to conduct. This excited pair can be thought of as an exciton, and if the binding energy of the excitons can be surmounted by an electric field across the layers on either side of the absorber layer where the carrier pairs are photogenerated, holes can be attracted to one side and electrons to the other [1]. Overall, electrons will flow in one direction - the definition of current generation.

PV technologies have taken on an ingenious variety of different forms in an attempt to achieve ever higher power conversion efficiencies (PCEs). Silicon-based solar cells, made of either mono- or polycrystalline silicon, remain the most widespread and most marketed today. Alternatively, PV technologies in the thin film category include dye-sensitised solar cells [2,3], $Cu(In,Ga)Se_2$ solar cells [4,5], organic solar cells [6], and perovskite solar cells [7-9], most of them named after a principal difference across them: the type of absorber layer utilised. This thesis will focus on the latter. Having long been in the spotlight, the lead halide perovskite absorber material for solar cells is inherently unstable if appropriate measures are not taken to protect it. It is prone to degradation

by exposure to humidity [10,11], ultraviolet light [12], and high temperatures [10,11], not to mention reactions with some of the layers placed against it in certain device stacks, where a stack denotes a series of nanofilm layers atop each other like in a PSC [10,13].

1.3 Background on Perovskite Solar Cells and Carrier Transport Layers

Perovskite solar cells have come up repeatedly in solar cell research over the past decade. Device stacks making use of perovskites as the absorber layer have experienced a more rapid rise in their efficiency than any other solar cell technology, with the current record having surpassed 24% light-to-electrical power conversion efficiency [14,15]. There is hope that PSCs could in the near future become the most efficient single layer PV technology available yet. That said, there are three factors that must be overcome before PSC technology can be marketed and become commonplace. Firstly, PSCs must present an advantage over existing silicon solar cells from the market. Although they have seen a rapid efficiency increase, a PSC device stack appropriate for mass production with a PCE comparable to that of silicon solar cells must be designed for their large-scale use to be justified. This has nearly been achieved at least in a lab setting, but to present a real advantage their cost or environmental impact must be lower than existing cells as well. Secondly, the perovskite absorber material is inherently unstable, and prone to damage due to exposure to moisture, ultraviolet light and oxidation [10-12]. This means PSCs do not yet meet the service life requirements of the market in the service environments they will have to face [15]. Finally, and perhaps least importantly, PSCs suffer from hysteresis effects, meaning that current-voltage curves in the forward and reverse voltage scanning directions do not overlap. However, this problem may be close to being solved, as research has been very successful in practically eliminating the hysteresis problem thanks to doping of transport layers (TLs) with aliovalent ions [16-18].

Perovskites are a crystal structure made up according to the chemical formula ABX_3, where A is usually an organic cation, B a metal cation, and X the placeholder for halide anions arranged in an octahedron around the B cation. Hence, they are organic-inorganic hybrid materials, shown in Figure 1. Some of the most frequent ions for A include methylammonium (MA^+) and formamidinium (FA^+) ions, for B they are lead or tin ions in an oxidation state of +2, and X is often Cl^-, Br^- or I^- [14,19]. Perovskites are incorporated into a device stack to make a solar cell from them, meaning that functional layers are added on either side, each on the order of tens to a hundred nanometres in thickness [10,20], to help with charge extraction and collection [1,14]. These other layers can also play a role in the protection of the perovskite [11], or improve interface contact between two layers.

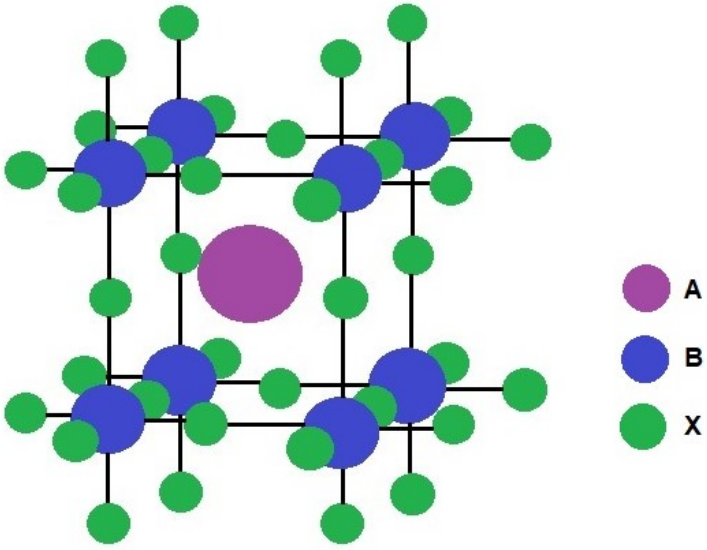

Figure 1: Perovskite crystal structure

Looking at only the functional layers, a PSC stack will have the general structure shown in Figure 2. The perovskite absorber layer will be sandwiched between two TLs: one for holes (the HTL) and one for electrons (the ETL) [14]. The HTL is typically a p-type semiconductor-like layer that will

transport holes to its electrode, and the ETL is an n-type layer that will do the same for electrons to the other electrode [20]. Finally, to terminate the stack on either side, there will be an appropriate electrode to collect the current at each end [14,20]. The anode would collect electrons from the ETL, and likewise for holes from the HTL to the cathode. There are two basic types of PSCs, with an inverted design also in existence for one of these types. The two types are planar and mesoporous PSCs, the former consisting of a simple series of nanofilms stacked on top of each other, and the latter being the same save a less abrupt transition between the perovskite layer and the ETL above it [14]. This is illustrated in Figure 2. A mesoporous PSC will have its ETL layer penetrate into its perovskite layer for more effective carrier extraction [15]. As well as being a separate film on top, the ETL will adopt a more porous morphology at one end, and have the perovskite layer merge into those pores [21]. Two architectures exist for planar PSCs: n-i-p and the inverted form p-i-n [14]. These names make more sense if we consider sunlight encountering them from left to right. In the n-i-p architecture, light would enter from the side of the anode and ETL, so these two would have to be largely transparent to visible and infrared radiation [15]. The light would then encounter the absorber layer, where most of the useful absorption occurs. This removes the transparency requirement for the HTL and cathode, as the useful light should have been absorbed by the time they are reached. It is the opposite in the p-i-n architecture, where the HTL and cathode should be transparent, a requirement that is no longer relevant for the ETL and anode.

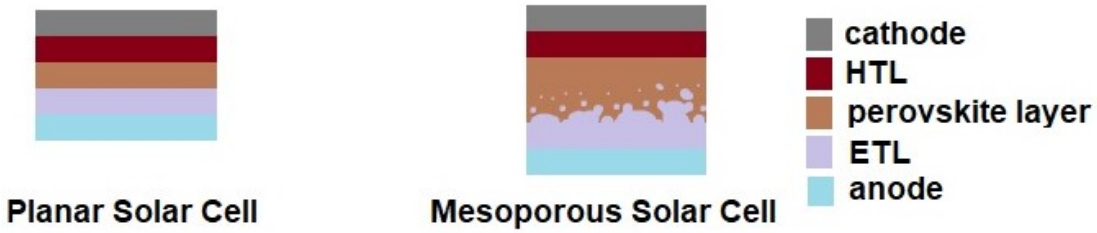

Figure 2: Planar vs. mesoporous PSC types

Some of the most common materials that have been used in research to produce PSCs of the n-i-p structure include fluorine-doped tin oxide (FTO) or indium-doped tin oxide (ITO) for the anode, titania (TiO_2) or zinc oxide (ZnO) for the ETL, perovskite materials that can contain organic ions such as FA^+ and MA^+ or inorganic ones like caesium (Cs^+), a polymer-based conductive HTL such as doped 2,20,7,70-tetrakis-(N,N-di-4-methoxyphenylamino)-9,90-spirobiuorene (a.k.a. spiro-oMeTAD) or poly[bis(4-phenyl)(2,4,6-trimethylphenyl)amine] (a.k.a. PTAA), and finally a cathode commonly made of silver or gold [14,19,22,23].

The material property requirements used to select the appropriate layer materials will be explained generally before bringing the focus to the ETL. First, a few simple requirements. As mentioned before, there is a transparency requirement for all layers that the sunlight is to cross before encountering the absorber layer. The layers must also be as stable as possible in the service environment, meaning they must be resistant to sunlight (including ultraviolet radiation), moisture, gases in the air, and temperatures of up to 75°C [24]. Reactions between layers should also be minimised so that they do not mutually shorten their service lives [10,13,14]. The more stable the layer materials, the longer the service life that the PSCs can reach, which is a barrier to be surmounted before they can become a marketable product. Another requirement concerns unwanted defects in the layers, which should be kept to a minimum. Point and extended defects in

the lattices of the layers, including interstitial or substitutional atoms, vacancies and impurities can all act as charge carrier trap sites. There are exceptions to this, for example vacancies in WO_3 assist with electron conduction, but generally defects are undesirable in solar cell materials [22]. The fact that these defects trap charge carriers inhibits their movement, negatively impacting conductivity [25]. The more charge carriers accumulate in an area of a semiconducting material, the greater the chance that they will recombine, decreasing carrier concentration, the open circuit voltage (V_{OC}) and the fill factor (FF), meaning less useful power obtained from the cell [16,21]. This is especially important at the interface between two layers, for instance between the perovskite layer and the HTL. Such interfaces between layers often have the highest defect concentrations in the devices, with the potential for agglomeration of carriers and recombination along the entire area of contact [26]. At the perovskite/HTL interface, holes would be lost as they recombine with photogenerated electrons in the perovskite layer instead of successfully crossing the boundary and being injected into the HTL. It is therefore imperative to the efficient working of the device that there is a quality interface between the different layers with as much contact area and as low a defect concentration as possible [9,16,26]. The same goes for the ETL/perovskite interface, and for the boundaries between the electrodes and their respective TLs. Sometimes, the device stacks are complexified with additional layers introduced between TLs and the absorber layer, specifically for interface passivation or trap site minimisation [26].

This leads to what may be the most important factor in selecting materials for PSC layers, especially for the TLs - the CB and VB energy levels of the TLs must be appropriately aligned with those of the perovskite layer to reduce carrier recombination [20]. To focus on the ETL, the CB minimum of the ETL material must not be too far above that of the absorber layer (it must be at least as negative as that of the absorber layer) relative to the vacuum energy level at which

carriers are completely free of the influence of the materials' potentials. This is portrayed in Figure 3. Otherwise stated, a CB offset that is too far positive is undesirable. If it was, electrons would encounter an energy barrier when trying to cross the boundary between the perovskite and the ETL. The V_{OC} would suffer as a result [27]. One of the purposes of the ETL is to provide a smooth energy transition for electrons crossing the barrier, so they can readily be extracted from the absorber layer. That said, the CB minimum of the ETL cannot be too far below (more negative than) that of the perovskite layer, in order to minimise the loss of carrier potential as the ETL is crossed into, as well as interfacial recombination. This would reduce the output voltage of the PSC device, decreasing the power output that it could deliver. It is therefore generally accepted that the CB minimum of the ETL relative to that of the perovskite layer should be negative, but by as small an offset as possible [9].

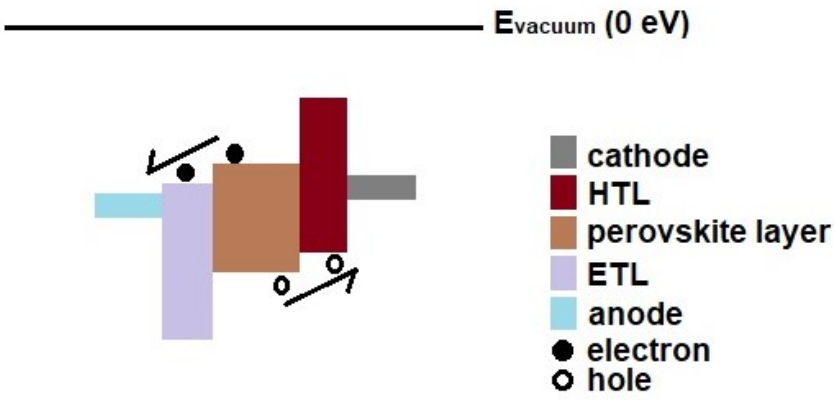

Figure 3: Relative arrangement of energy levels or bandgaps in some PSCs. For the ETL, perovskite layer and HTL, the bottom of the rectangle depicts the VB maximum and the top is the CB minimum. For the ETL a positive VB offset and negative CB offset is shown. For the HTL a negative VB offset and positive CB offset is drawn.

This is the opposite for the VB alignment between the ETL and absorber layer. Here, it is desirable to have a positive VB offset, so to have the ETL's VB maximum more negative than that of the

perovskite. This is to prevent the extraction of holes so that they do not end up in the ETL. Holes are transported in the VB, and unlike electrons the more negative the energy level that they occupy, the higher their energy state. This means that with a positive VB offset, holes are faced with an energy barrier upon nearing the ETL, decreasing the probability of them entering it. Thus the ETL is also called the hole blocking layer, and the HTL the electron blocking layer. The layers on each side of the perovskite are meant to block one carrier and accept the other, creating an electric field across the whole device such that only a one-way flow of each carrier type is permitted, with each type drawn to the opposite direction to produce a current. Materials for the HTL are therefore chosen such that they will have a small but positive CB offset with the absorber layer, and a small but negative VB offset with it (although a slightly positive one on the order of +0.1 eV works just as well for many HTLs), to block electrons and accept holes [20].

1.4 Suitability of Transparent Conductive Oxides as ETLs

Transparent conductive oxides (TCOs) are very well-adapted as ETLs for perovskite solar cells; a look at their unique combination of properties explains this. This class of materials was not named arbitrarily: they are metal oxides that are transparent to infrared and visible light, but also have some properties of semiconductors. They are electrically conductive and can boast high charge carrier mobilities [28]. That said, their bandgaps are not as narrow as semiconductors (3-4 eV compared to about 1 eV), enabling them to accept charge carriers without being plagued by poor carrier lifetimes due to rapid recombination rates [14]. On top of being permeable to infrared and visible radiation, two regions of the electromagnetic spectrum that PSCs can produce power from, many TCOs block ultraviolet radiation, which is useful for n-i-p PSCs. This is due to perovskites being sensitive to ultraviolet frequencies [12], and so a TCO ETL could provide additional protection in case any UV light makes it through a crack in the glass layers that would likely serve

as the front layer of a PSC product, as glass already blocks UV light. Using suitable TCOs as ETLs can therefore provide a sufficiently conductive path from the perovskite absorber material to the front electrode that is protective and stable, with low recombination rates in the TCO material itself, and with VB and CB energy levels that are appropriate for use with perovskites [12,17]. The electron mobilities in some TCOs are very respectable, with SnO_2 exhibiting values of up to 250 $cm^2/(Vs)$ [14,28]. ZnO, another ETL material favoured for its performance, has a lower mobility of up to 200 $cm^2/(Vs)$ [14].

The details of SALD will be unveiled in section 1.6. For now, it is sufficient to say that it is a convenient method to produce TCOs that are very uniform, pin-hole-free and of high quality, with flat end surfaces when deposited on a flat substrate [11]. This means that on top of the inherent advantages of TCOs just mentioned, the choice of SALD as a deposition method to grow them offers additional benefits. An SALD-grown TCO layer should be poorer in carrier trap and recombination sites at the interface (due to the flatter upper surface compared to, say, a spin-coated film), and have highly uniform material properties. This upper surface is the one that would contact the perovskite layer, and making good, uniform contact with it is essential to avoid interface carrier recombination and to decrease hysteresis. Moreover, the quality of the TL that the perovskite layer is deposited on impacts the degree of crystallisation and morphological quality of the perovskite, which are important in determining performance parameters such as the wavelength range that will be absorbed [28]. A lower defect concentration would mean that SALD-grown ETLs should theoretically benefit from longer charge carrier lifetimes and higher electron mobilities than similar layers grown with other methods (except perhaps ALD, but then the latter means a whole new set of limitations, see section 1.6).

1.5 Benefits of Doping Transparent Conductive Oxide ETLs

Doping of a material is to add atoms of another element into it during its fabrication process to give it enhanced properties for an application. Doping of TCO ETLs has been tried extensively and has led to promising results. Doping cobalt into TiO_2 has led to increases in V_{OC} and PCE without worsening solar cell hysteresis [21]. It also improved the carrier mobility of the TiO_2 and shifted its band structure upwards, improving charge extraction from the perovskite [21]. Doping TiO_2 with metals of a higher electronegativity than Ti was found beneficial thanks to the upshifting of the CB minimum that it provides, boosting the V_{OC} of PSCs using it as an ETL [21]. Doping hafnium into ZnO was found to increase its conductivity and carrier concentration as well as improve crystallinity, as long as less than 7% hafnium was added [6]. Al and Mg doping into ZnO has also let to advantages desirable for PSC ETLs [6]. Regarding SnO_2 doping, lanthanum addition increased the V_{OC} of PSCs using it for an ETL, and 2.5% of La content was sufficient to bring about significant PCE improvements [17]. The solid conductivity of alkali ions such as Li^+ or K^+ reduces the series resistance of cells, increasing V_{OC} [17]. The list goes on: among others, n-type Cd^{3+} or Y^{3+} to create donor centres in SnO_2 to boost charge mobility, and anion doping to increase conductivity and reduce energy band offset with adjacent layers have both been implemented [17]. In summary, the addition of even a few atom % of a broad variety of foreign elements can bring notable improvements to the morphology and optoelectrical properties of a TCO nanofilm for this application. It also allows for upshifting or downshifting energy bands, to favour transfer of electrons from one layer to the next by better matching the electrical potentials of the TCO with another layer of a thin film device that one may not have the luxury to customise or dope as freely as the TCO layer.

Ternary metal oxides like ZTO take this idea of doping further: more than doped oxides, they are an oxide of two metals, with both present in very significant amounts. Ternary oxides are concerned with a much broader compositional variation than simply doping a few atom % of a foreign element into a matrix; as they can have a composition anywhere between the two extremes represented by each of the pristine native oxides. This should in theory allow for ZTO to have a much more customisable material property space, comprising those of ZnO, of SnO_2, any in between, and possibly even some outside that range [1]. For example, bandgaps outside the range of ZnO's (3.3 eV) and SnO_2's (3.8 eV) may be possible at specific ZTO compositions, especially if both microcrystalline and amorphous film microstructures are considered [5,29,30]. SnO_2 is regarded as one of the top pure metal oxide performers for ETL applications. ZnO is lagging just behind, if at all, since it has been argued that it is at least as performant as SnO_2 [13]. One of the main concerns with the use of ZnO as an ETL is its incompatibility with perovskite materials [1,13]. That said, it has been demonstrated that the source of this problem is a reaction between the oxide and the MA^+ ion present in certain perovskites [13]. If the perovskite is made without this ion, as is the case in many promising perovskite materials, the problem is eliminated, making ZnO a great ETL choice as well [13]. The customisable ternary oxide of arguably the two most performant ETL oxides that is ZTO is therefore very worthy of study, and ZTO is expected to be a more performant ETL than either of its constituent oxides [1]. The use of ZTO as a PSC ETL has been investigated, though not in many studies. The properties of sputtered ZTO films have been studied previously, and those properties were used to simulate the use of ZTO with equal contents of Sn and Zn as a PSC ETL. A PCE of 24%, a V_{OC} of 1.13 eV and a short-circuit current (J_{SC}) of 23.2 mA/cm^2 were calculated by the software using the properties of ZTO sputtered at 300°C as inputs for the simulated ETL's properties, all very respectable numbers on the higher end of the literature

values [31]. Slightly lower values and a PCE of 19% were found for bilayer ETLs used in PSCs - with a layer of spin-coated ZTO against one of SnO_2 used together. The cells showed superior performance and stability, with the best performance seen when the Sn and Zn contents were equal in the ZTO layer [1]. Spin-coated Zn_2SnO_4 - a crystalline form of ZTO - has been used as an ETL in another study in a mesoporous PSC. Although the PCE from that study was closer to 13%, superior charge transfer to the ETL was observed, and the hysteresis was negligible [18].

1.6 Background on Spatial Atomic Layer Deposition

In order to understand SALD, it is first necessary to understand its parent: traditional atomic layer deposition (ALD). ALD is a chemical reaction-based nanofilm deposition technique that finds numerous applications in the fields of nanoelectronics and optics, able to produce coatings with exceptional uniformity and a low concentration of pin-holes compared to sol-gel methods, where there is far less control over the reaction [25,32]. Gaseous chemical precursors are drawn into a chamber containing the substrate that is to be coated. This is performed in a vacuum to limit any undesirable reactions or physical interactions that may occur with the interference of atmospheric gases. The process is also done in a sequence, which is useful for depositing films that are to be formed by the reaction of two (or more) precursors. A typical ALD deposition process would take place in the following sequence, depicted in Figure 4 for the case of tetrakis(dimethylamino)tin(IV) (TDMASn) reacting with water to form SnO_2. The substrate is exposed to the first precursor for a length of time usually on the order of a few seconds. It is of interest to expose the substrate for enough time to have its surface uniformly coated with a single layer of precursor molecules that may be physisorbed or chemisorbed onto the surface. In true ALD conditions, this is the ideal case [33]. The interval of exposure to the first precursor is followed by a purging interval that usually lasts a few seconds longer. In this step, the substrate

surface is exposed to an inert gas to both remove any precursor that may have adhered in the vicinity of the surface but is not as strongly bonded as the chemisorbed molecules that are going to form the film, and to purge the ALD reaction chamber of any of the first precursor that may otherwise interfere with the next reaction step [34]. The substrate is then exposed to the second precursor. This deposits a layer of the second precursor onto that of the first, reacting with it and forming a first monolayer of the material that is to be deposited [33]. A purge step similar to the first is repeated, and the overall process made up of the same four steps is repeated until a film of sufficient thickness is deposited, with each of these cycles depositing about 1 angstrom of material [33,35,36]. The substrate is usually heated to encourage the reactions that will produce the films [37].

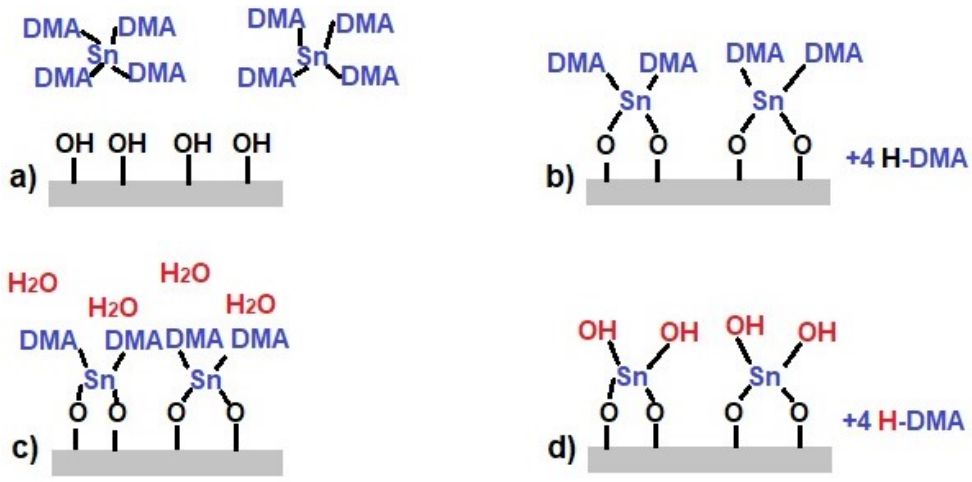

Figure 4: ALD reaction of TDMASn with water for the case of 2 ligands reacting with a hydroxyl-terminated surface. a) The substrate surface is exposed to the precursor. b) TDMASn chemisorbs onto the substrate (the 1st half-reaction) releasing two of its DMA ligands per molecule. The chamber is purged of excess TDMASn. c) Water is introduced into the chamber. d) The water reacts (the 2nd half-reaction) releasing the remaining TDMASn ligands from the film surface and restoring the hydroxyl-terminated surface for further reactions. The chamber is purged of excess H_2O.

One class of materials that has been extensively deposited with ALD is metal oxides [11,14,15]. For instance, in the deposition of ZnO, the substrate would be repeatedly exposed to precursors that would bring each of the desired atoms into the film: a zinc precursor (usually diethylzinc, DEZ), and an oxidising agent (such as water or H_2O_2). The reactants are selected such that their reactions with both the substrate and with each other on the growth surface cause the parts of their molecules that are not of interest to leave the reaction sites rather than become a part of the film, leaving behind only the atoms of interest [38]. It does happen that these residue ligands from the precursors remain in the films, an effect that has been shown to diminish with increasing substrate temperature during the reaction [34]. In the case of TDMASn and SnO_2, this is believed to be because the precursor decomposes more efficiently at more elevated temperatures [39].

More recently, SALD has emerged as an alternative ALD process. SALD is extremely well-suited to the deposition of metal oxides, with the technique having been used to grow a whole range of them including ZnO, Al_2O_3, SnO_2, ZTO, AZO, WO_3 and Cu_2O [11,29,40]. The technique is named 'spatial' since instead of separating substrate exposure to the reactants through time, it is done through space. At a given time, the substrate is exposed to all of the reactants, but different areas of it are exposed to different ones, and there is a relative motion of the substrate and the reactor head so that each area cycles through exposure to each of the reactants as they would in traditional ALD. The reactor head is central to the SALD process, usually consisting of a solid component with several gas feed tubes as the input and parallel adjacent thin slits for an output, situated less than a millimetre above the reaction surface. Each slit that carries a reactant gas of importance to the reaction will have slits releasing an inert gas (nitrogen or argon) on either of its sides, keeping each reactant spatially separate to minimise any reactions other than on the surface of interest. Exhaust slits between each gas or reactant-emitting slit provide outlets for the gases supplied,

aiding with film uniformity [33]. Such a reactor head is shown in Figure 5, though it has differences with the one used in this project, as will be explained later.

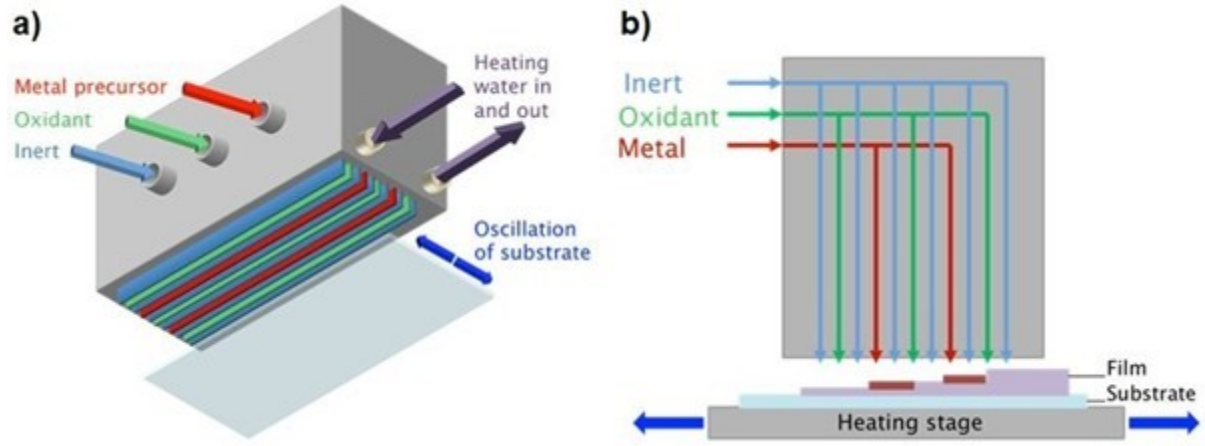

Figure 5: Depiction of the SALD process using a reactor head above a heated stage. a) 3D model & b) cross-sectional view [41].

It is from the use of a reactor head that the two huge advantages of SALD over ALD as a nanofilm deposition method are born. Firstly, it is quicker due to the elimination of the need for purging steps. All of the gases can be blown out continuously from chemical precursor bubblers thanks to the shielding curtains of gas produced by the configuration of the reactor head slits, to keep reactants separate [33]. Secondly, and perhaps most importantly, the significant energy, space, and financial requirements of entertaining a vacuum environment for reactions are fully eliminated - for SALD is a process performed at atmospheric pressure, humidity and air mix conditions (at least for oxide deposition). From this it can be understood why SALD would be the deposition technique of choice for a material if it is able to produce it. Compared to available alternatives, it is inexpensive, simple to implement, fast (an order of magnitude quicker than ALD in terms of growth rate per unit time, simply from elimination of the purge steps), appropriate for use with a broad variety of precursor chemicals and oxidising agents, and is able to produce high quality films

with a lower defect concentration as the monolayer-by-monolayer deposition mode from ALD is usually maintained [42].

These important advantages of SALD entrust it with the potential to be used as a high-throughput method to produce nanofilms, appropriate in a mass production setting. If PSCs are marketed in the near future, those investing resources to bring them to the public may be making a mistake to ignore the great advantages that SALD can provide them with, depending on the materials they end up selecting for the layers of their device stacks [42].

Although SALD usually produces amorphous material layers, there is a correlation between substrate temperature during the deposition and film crystallinity, providing freedom to customise the materials grown [37]. The technique has also been used to dope its nanofilms by introducing a low concentration of another precursor. A reactor head may also contain several channels for precursors plus that of the oxidising agent, allowing for deposition of materials containing more than two elements. Similarly, the one other study found on SALD-deposited ZTO was by co-injection SALD; where the same precursors as in this study were used but injected into the same reactor head slit. Despite flow rates as high as 900 sccm through the tin precursor bubbler, the highest Sn content that was attained was only 26% [29]. Moreover, although some connections were made with $Cu(In,Ga)Se_2$ solar cells, the ZTO films were not investigated in the context of solar cells in detail [29]. Thus, the project carried out here builds on this past study on SALD-deposited ZTO by presenting an alternative non-co-injection ZTO growth method that achieves a much broader range of compositions (Sn contents of 30-97% compared to 0-26%). This is achieved without needing extremely high flow rates through the bubblers, and so likely by consuming less precursor for similar film dimensions. The emphasis here is more on SALD-grown ZTO for solar cells, more specifically for PSCs, which has not been investigated (to the best of our knowledge).

The chemical equations for the ALD reactions of DEZ to form ZnO ((1) and (2)) and for TDMASn to form SnO_2 ((3) and (4)) with H_2O are now shown [38]. 'Et' represents an ethyl ligand and 'DMA' a dimethylamino ligand. An asterisk marks a surface-bonded species. Both of these two sequences of half-reactions occur in the SALD deposition of ZTO.

$$OH^* + Zn(Et)_2 \rightarrow O\text{-}Zn(Et)^* + H\text{-}Et \quad (1)$$

$$O\text{-}Zn(Et)^* + H_2O \rightarrow O\text{-}ZnOH^* + H\text{-}Et \quad (2)$$

$$(OH)_x^* + Sn(DMA)_4 \rightarrow (O)_xSn(DMA)_{4-x}^* + x(H\text{-}DMA) \quad (3)$$

$$(O)_xSn(DMA)_{4-x}^* + (4-x)H_2O \rightarrow (O)_xSn(OH)_{4-x}^* + (4-x)(H\text{-}DMA) \quad (4)$$

CHAPTER 2: EXPERIMENTAL METHODS

2.1 The SALD Apparatus Used

The ZTO nanofilms were deposited using a custom-built SALD system. Various mass flow controllers (MFCs) were used to control the flow of nitrogen gas from a common cylinder through the different lines (of steel or polymer tubing) of the SALD - one for tin, one for zinc, and one for water, among other lines. Each metal line had a bubbler containing the precursor for that line, with a bubbler bypass tubing assembly to be able to purge the lines without flowing through the bubblers, as depicted in Figure 6. Further down each line, there was another gas inlet controlled by another MFC: an N_2 carrier line to merge with the flow from the bubbler and carry it forward to the reactor head. The reactor head is the component just above the heated moving stage on which the SALD reactions take place. The heated stage was made to oscillate back and forth so that different regions of the substrate could experience sequential exposure to each of the reactants necessary to produce the nanofilms.

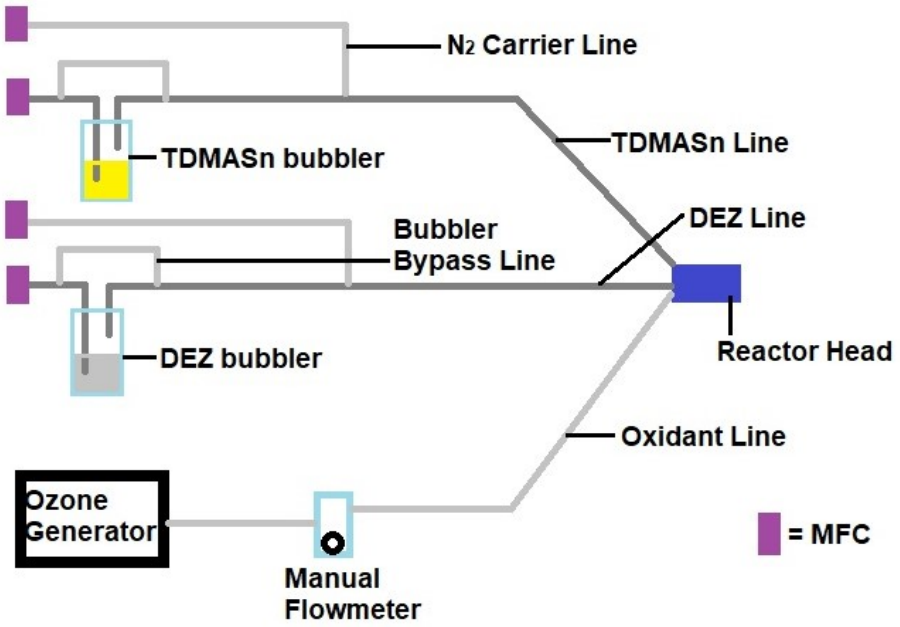

Figure 6: Schematic showing the arrangement of SALD reactant lines used. Valves were placed along the lines to better control flow (not shown).

The reactor head consisted of a steel block holed with channels for each of the gas lines going into it, ending in parallel slits on the bottom side facing the heated stage, similar to that depicted in Figure 5. The slits were used as illustrated in Figure 7. The Metal-1 precursor had a single outflow slit (yellow), while the Metal-2 precursor had two slits dispensing the same gas mixture (orange). Slits for pure N_2 flow were located between each of the reactant slits to provide gas curtains, both to keep the reactants separate and to shield them from gases in the atmosphere, as well as performing the equivalent of the purging step in traditional ALD by removing precursor molecules that are not adsorbed from the nanofilm surface. The system also had regular exhaust slits adding the capability to draw gases out and away from the reaction site using the suction provided by a small motor. That said, this feature was rarely used in the experiments for this thesis.

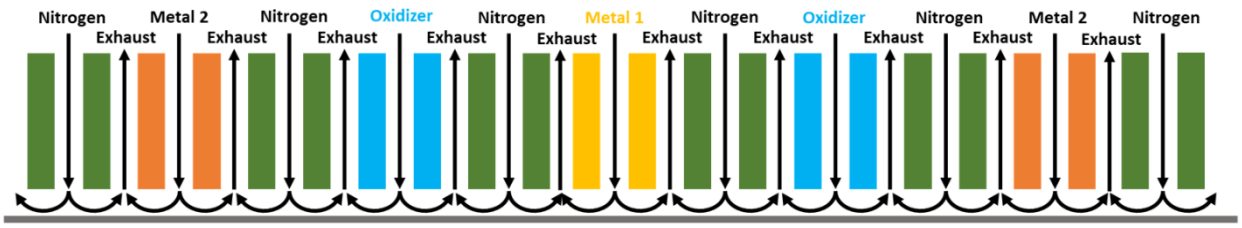

Figure 7: Arrangement of SALD reactor head gas slits used

2.2 ALD vs. CVD Deposition Conditions

ALD and its cousin chemical vapour deposition (CVD) are so similar that they can both take place in a set-up like the one used in these experiments, simply from varying the deposition parameters slightly. During ALD, there is no intermixing of the reactants in the gas phase, and the substrate is exposed to only one of the reactants at a time. However, in CVD the deposition conditions are such that at any given time, there are areas of the substrate exposed to more than one reactant simultaneously, such as ozone and DEZ. This translates into both half-reactions being able to occur for as long as the exposure lasts, leading to an end to monolayer-by-monolayer deposition, and to higher growth rates [43]. The most relevant parameters here are the spacing between the reactor head and the substrate on the stage, and the flow rate of the N_2 curtains between the reactant slits. These parameters are key in this context since they are the main ones affecting the degree of intermixing of the reactants, making all the difference between a more CVD-like and a more ALD-like deposition process. In a true ALD process, there is no mixing of the reactants in the gas phase, and only the monolayer of adsorbed precursor reacts with the oxidant on the film. In this way, monolayer-by-monolayer deposition is achieved, with fine control over the thickness and very abrupt nanofilm edges. But if the reactor head spacing is too wide (such as 1 mm), or the N_2 curtain flow too weak, CVD can occur. For the experiments of this project, although the aim was to produce films by SALD, the ALD window of deposition conditions for the ZTO recipes used

(those in which nanofilms are deposited in the ALD fashion) was not specifically investigated. The ZTO recipes were judged appropriate for the project to continue once quality films were achieved. This means it is possible that the ZTO nanofilms were in fact deposited by SCVD (spatial CVD) or by a combination of SCVD and SALD. Regardless, their quality is defended later, evidence that if they are SCVD films, the technique can produce quality films even without the monolayer-by-monolayer deposition characteristics of SALD. That said, in section 3.3 the growth per cycle of some of the films deposited will be estimated in order to determine whether the deposition of ZTO achieved here was more of an SCVD-like or SALD-like reaction, since the two processes have notably different deposition rates [4,43]. The argument that SALD was the principal deposition process will be defended.

2.3 Deposition of ZTO Nanofilms by SALD

SALD deposition of ZTO nanofilms was carried out with the apparatus detailed in section 2.1, using TDMASn and DEZ as the chemical precursors for tin and zinc oxides respectively, which were reacted with ozone as the oxidant. The ozone generator used was an Absolute Ozone Atlas 30 UHC which was used with its output dial set to '75'. Depositions were carried out on 7 x 7 cm borosilicate glass substrates maintained at 165°C for the duration of the depositions, and the TDMASn bubbler was heated to a temperature between 55 and 65°C. According to most suppliers of the chemical, this range is above its boiling point, and indeed fumes were often visible inside the glass bubbler when it was being heated. This was taken to be a good sign, and days on which the depositions were most successful were usually ones in which some extent of TDMASn boiling had been observed. The nitrogen flow rate through the bubblers are the parameters that were used to vary the composition of the ZTO films produced, and will be discussed in much greater detail in later sections. They were varied in the range of 75-300 sccm for the tin bubbler and 5-50 sccm

for the zinc one. For each of the metal precursor lines, the flow from the bubblers was made to join up with a carrier flow of N_2 gas before sending it to the reactor head. This can be useful to balance the flow rate coming out of each slit in the reactor head. The carrier flow rate for the tin line was 250 sccm, and the equivalent value for the zinc line was 175 sccm. The Metal-1 channel was used for the Zn line, with one slit delivering DEZ out of the reactor head, and the Metal-2 line was used for the tin, with twice as many slits delivering TDMASn to the substrate (Figure 7). Ozone was delivered through the two oxidiser slits at a rate of about 325 sccm through each slit, with an approximate concentration of 280 g/Nm^3 (grams of ozone per cubic metre at standard pressure and temperature), balanced with a mixture that was 7.5% N_2 and 92.5% O_2 by volume (prior to some of that oxygen becoming ozone). The speed used for the oscillation of the substrate back and forth relative to the reactor head was 4.5 cm/s, and the width of the gap between the substrate and reactor head was between 150 and 200 microns. The exhaust channels in Figure 7 did not have gas actively drawn through them to evacuate the unreacted or excess gases from the substrate vicinity, although they may have played a passive role in their evacuation. The flow rate out of each of the N_2 curtain slits was 75 sccm.

As part of the project, deposition of SnO_2 was also attempted (with a similar process but without the use of DEZ). It should be noted, if the experience with our SALD system is to be believed, that deposition of SnO_2 from TDMASn is significantly less straightforward than the literature would lead one to think. Great difficulty was had in depositing SnO_2 either using water as the oxidant, or without the assistance of at least a small amount of DEZ flowing through the other metal channel, which seemed to assist in the deposition process of TDMASn and its reaction on the substrate or film surfaces. A similar effect has been reported before for ALD of Zn-containing oxides [44]. It is also known among researchers in the field that TDMASn can take a significant saturation time,

or time spent with the Sn line in the same flow and temperature conditions as it would be in during a successful deposition, before any Sn begins to be incorporated into a film. During this warm-up time, the precursor flows through the tin channels of the system leading up to the reactor head, so that the line is coated with at least a certain concentration of precursor all the way up to the reactor head. The nanofilms deposited for this project with any meaningful Sn content were usually deposited after a minimum of a couple of hours of saturating the Sn line. For the entire time that the system was in use (in between depositions), a certain flow rate was maintained constantly through the TDMASn bubbler - a flow rate of about 75 sccm, lower than that which would have been used during a deposition. Such were the conditions under which Sn-containing ZTO depositions were the most successful in our system, although saturation of a tin line may take less time if the flow rate through it is greater or if the line is heated along its length. Thus, certain difficulties of SnO_2 deposition with a lab-scale SALD system from TDMASn may be somewhat understated in the literature - difficulties which ZnO deposition from DEZ, for example, does not share.

2.4 Explanation of Characterisation Methods and Performance Tests Used

2.4.1 Scanning Electron Microscopy & Energy-Dispersive X-ray Spectroscopy (EDX)

An SEM is a powerful tool able to render black-and-white images of down to nanometre-scale features and the morphology of a sample with detailed resolution [45]. A great variety of solid samples can be examined by it, although it is preferred if the samples are conductive to prevent surface charging from the electrons of the beam being unable to evacuate the area being examined. An SEM works by firing a focused electron beam at the sample with an electron gun [45]. This is possible for instance by heating a tungsten filament, causing thermionic emission of electrons to be focused into a beam by apertures and lenses [45]. Information from up to 5 microns deep in the

sample can be probed, and the beam of electrons causes the emission of photons and electrons from the interaction volume around where the beam hits the sample [45]. What is usually carried out to collect images from SEM is the detection of secondary electrons, which are those removed from the closest shell to the nuclei of the specimen atoms through interaction with the primary electrons from the beam [45]. There are also backscattered electrons to be collected - those reflected by the specimen's atoms [45]. Detecting the latter is mostly useful when needing to differentiate between heavy and light elements at the surface: the higher the atomic number of the element, the more electrons it will backscatter, brightening the image [45].

EDX is a characterisation technique performed in an SEM, taking advantage of the fact that examining a specimen in an SEM will cause it to generate X-rays [29,45]. Emission of a secondary electron from an atom will result in an electron from the outer shells of that same atom filling the vacancy in the core energy level [29,45]. The energy lost by the electron during the transition to the core shell is given off as an X-ray of a characteristic energy which is a function of the element [29,45]. This allows for the X-ray intensities as a function of energy to be collected and displayed in a spectrum, with a peak for each X-ray energy detected [29,45]. Which elements are present can be discerned from the positions of the peaks, and the peak intensities can be related to the proportion of a particular element in the specimen [29]. The device used here was a ZEISS Ultra Plus SEM.

2.4.2 X-ray Photoelectron Spectroscopy (XPS)

XPS is a widespread surface chemistry and composition analysis technique in which the sample is irradiated with monochromatic X-rays [29,45]. If the latter are of sufficient energy, they will cause the ejection of core electrons from the material surface (the photoelectric effect) [45,46]. The kinetic energy of these outgoing photoelectrons is measured by a detector, and as energy must be

conserved in the process, the binding energy that held an electron at its energy level in the material can be calculated from knowing the kinetic energy of the photoelectron and that of the incoming X-rays, according to equation (5):

$$E_{kinetic} = hf - E_{binding} - \Phi \quad (5)$$

where Φ is the work function of the material surface and hf represents the energy of the incoming X-ray photon [29,45]. The unique electron configuration of each element allows for discerning them when measuring the photoelectrons' energies [29]. The process is usually performed in a near-vacuum environment to prevent ambient gases inhibiting electron movement, but there are exceptions to this [45,46]. XPS can only provide information from a few nanometres deep in the sample due to the outgoing electrons having a very short mean free path in solids [45,46]. XPS yields a spectrum of electron intensity against the binding energy, providing information on composition, oxidation states, and adsorbate coverage, and is especially useful for yielding relative element concentrations [29,46].

The XPS system used in this project was a VG Scientific ESCALab 250 system. An Al Kα X-ray source was used and analysis of the spectra was done with the CasaXPS software, in which the carbon C1s peaks were aligned to 284.6 eV.

2.4.3 Spectroscopic Ellipsometry

Ellipsometry can be sensitive to a single monolayer of material on a substrate, and is an extremely accurate thin film analysis method with very reproducible results when used correctly [29,47]. A variety of optical and physical parameters can be determined from it. These can be, if they are relevant to include in the model used in the software to describe the film: thickness (including thicknesses of individual layers stacked atop one another in a complex nanolaminate structure),

refractive index and extinction coefficient (which together make up the complex refractive index), bandgap, and surface roughness [47,48]. These parameters are not measured directly, but calculated from other measurements made by the ellipsometer [48]. What the latter does measure are optical parameters related to the polarisation of light being shone onto the film and being reflected off of it [29,47]. Incoming linearly polarised light will usually be reflected as elliptically polarised light once it leaves the sample [29]. Both the light rays from the source and those reflected can be resolved into 'p' and 's' components, corresponding to those in the plane of incidence and perpendicular to it respectively. An ellipsometer will measure Ψ and Δ, the ratio of amplitudes and difference in phase respectively for the p- and s-polarised beams after reflection from the sample [47,48]. Both of these are determined as a function of wavelength. To get use out of these values, a model of the film being measured is built in an ellipsometer software to describe its layers and substrate. The optical parameters that have been selected for evaluation for the film (say refractive index and thickness) are then varied through iterative steps until the simulated Ψ and Δ are best matched to the measured versions of these functions at the wavelengths used [29]. At that point, the error has been minimised, and the refractive index and thickness will have been evaluated with accuracy.

In the work undertaken here, the ellipsometry data for the ZTO films was fitted using both Tauc-Lorentz and Cauchy models. Although ZnO and SnO_2 along with other semiconductor-like materials are commonly modelled using a Tauc-Lorentz optical model, and the use of a Cauchy one is more appropriate for alumina and other materials transparent to visible light, a good fit was found for both types of models for the ZTO nanofilms produced [49-51]. Moreover, the two dispersion models were found to be consistently in solid agreement over the thicknesses of the

films. As such, results from fits of both of the models will be included for completeness. The ellipsometer model used was a Film Sense FS-1.

2.4.4 X-Ray Diffraction

X-ray diffraction (XRD) is a well-established X-ray characterisation technique allowing identification of solid samples through determination of the crystal phases present in them. To carry it out, an X-ray source, usually consisting of copper, is used to generate a beam of monochromatic, coherent X-ray radiation that the sample is exposed to [29,45]. The planes of atoms in the crystals of the sample will reflect the X-rays according to the conditions of Bragg's law, shown in equation (6) and in Figure 8:

$$n\lambda = 2d\sin\theta \qquad (6)$$

where n is an integer, d is the interplanar distance between the atomic planes of the phase of interest, θ is the angle between those planes and the incoming radiation beam, and λ is the wavelength of the source's radiation [29,45]. The X-rays used are commonly copper Kα radiation [40,45]. Bragg's law determines the conditions under which the X-rays reflected by atomic planes in the sample will interfere constructively - when the path difference between the rays scattered by consecutive parallel atom planes (the right side of equation (6)) is equal to a whole number multiple of the radiation's wavelength [29,45]. The periodicity inherent to a crystal structure is therefore a requirement for constructive interference, and by extension obtaining a signal from the sample under examination. Under conditions at which Bragg's law's requirements are not met, destructive interference of the beams scattered from consecutive planes in a crystal will occur. Another consequence of Bragg's law is that only certain angles of the incoming X-ray beam relative to the sample surface will produce a signal for the detector, allowing for specific peaks to be interpreted as a signature of the crystalline phases (and therefore materials) present in the sample as the angle

of the incoming radiation is varied to yield a graph of intensity against 2θ [29,45]. The latter quantity is the angle between the incoming and reflected X-rays [45]. The relative heights of the peaks provide insight into the composition of the material [29]. For thinner samples with a thickness in the nanometre range, the standard method of performing XRD measurements will probe the sample too deeply, so that the resulting spectra will include some signal from the substrate. Thus as part of this project only grazing incidence XRD (GIXRD) was used to avoid this problem; an XRD technique using very low angles of photon incidence (such as 1°) to only yield a signal from near the top surface of a sample [45].

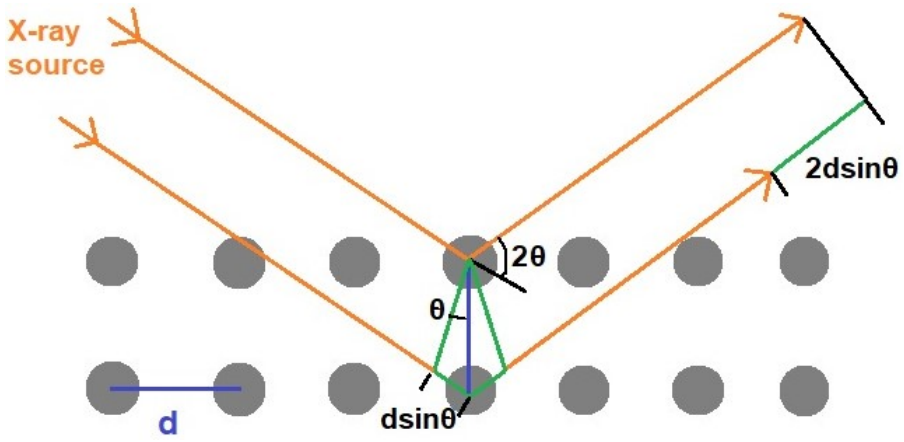

Figure 8: Bragg's law - reflection of X-rays from the atomic planes of a crystal

In XRD, the peak width is an indication of the crystallinity of the sample, with sharp thin peaks pointing towards a more crystalline sample, whereas peak broadening is expected for low-crystallinity samples. The Scherrer equation (equation (7)) can provide a lower limit of the mean crystallite size in a micro- or nanocrystalline film:

$$x = \frac{K\lambda}{W cos(\theta)} \qquad (7)$$

where θ is the diffraction angle at which the peak of interest occurs, W is the full width at half maximum of the peak, $\boldsymbol{\lambda}$ is the wavelength of the X-rays used, K is a unitless shape factor (commonly 0.89 in the case of spherical crystals) and x is assumed to be the average size of crystallites [29,52].

GIXRD was performed in a PANalytical X'PERT PRO diffractometer system using Cu Kα radiation with a wavelength of 0.15406 nm. The range of 2-theta values was from 20 to 90° with a scan rate of 0.02°/s, and the omega angle was 0.0001°.

2.4.5 Atomic Force Microscopy

An atomic force microscope (AFM) makes use of an atomically sharp tip with dimensions in the nanometre range on the end of a flexible cantilever with a reflective top surface [53]. Usually, laser light is shone onto this top, reflecting the laser onto a detector. The detector uses the position of the reflected laser spot to determine the precise position of the sharp tip along with the extent of deflection of the cantilever [53]. The sample whose surface is under examination rests atop a mobile stage, which can be moved laterally in two dimensions while the tip is moved in the up-and-down direction in order to maintain a constant separation with the sample surface [53]. This produces a three-dimensional representation of the physical features and roughness of the sample surface.

In this project, the AFM used was a Bruker Dimension FastScan AFM, and data analysis and presentation was carried out using NanoScope Analysis software version 1.8.

2.4.6 UV-Vis Spectroscopy & Tauc Plots

An ultraviolet-visible-near infrared (UV-Vis-NIR) spectrometer is equipped with a set of lamps, for example a tungsten one and a deuterium one, each of which are suitable for producing radiation

in a specific part of the electromagnetic spectrum with which samples will be illuminated. A tungsten lamp may be used to produce radiation of wavelength greater than about 300 nm, while the deuterium one is better suited to wavelengths shorter than 300 nm, so that together they enable the spectrometer to expose a transparent or translucent sample to all frequencies in the regions of the spectrum that the device is named after. Many UV-Vis spectrometers can yield spectra for all three of transmittance, reflectance and absorbance of a sample as a function of the illumination wavelength. The absorbance calculation is based on the Beer-Lambert law [29,45]:

$$I(x) = I_0 e^{-\alpha x} \qquad (8)$$

where I_0 is the light intensity of a particular wavelength before interaction with the sample, $I(x)$ is the intensity at depth x into the sample, and α is the absorption coefficient at that wavelength for the material being analysed [29,45]. For a solid film, the absorbance is equal to αx, and therefore increases with the thickness of the film. The transmittance, or proportion of light intensity that passes through the sample, is the fraction I/I_0. If the detector is set to collect light that is reflected from the sample rather than that which has passed through it, that same fraction becomes the reflectance [45].

A Tauc plot can be used to graphically estimate the bandgap of a film that is light-absorbing to an extent, assuming either a direct or indirect electronic transition upon absorption, starting with an absorbance spectrum as a function of light wavelength. It is based on Tauc's law, expressed here in a form convenient for graphing (equation (9)):

$$(\alpha h\nu)^{1/n} = B(h\nu - E_g) \qquad (9)$$

where α is the absorption coefficient (which will vary with the frequency), ν is the frequency, h is Planck's constant, B another constant, E_g the bandgap, and n an exponent whose value is adjusted

depending on whether a direct or indirect bandgap is assumed for the material under examination. It takes on a value of 0.5 in the case of a direct bandgap and 2 for an indirect one [52]. If left side of equation (9) is plotted on the vertical axis against *hv* on the horizontal, the bandgap becomes the x-value of the point of intersection of the x-axis with a line extended from the linear portion of the curve towards the horizontal axis [52]. The absorbance spectrum enters the calculations as it yields the array of absorption coefficients to be used when combined with the nanofilm thickness (equation (10)):

$$\alpha(v) = \frac{2.303 \times A(\lambda)}{d} \qquad (10)$$

where $A(\lambda)$ is the absorbance as a function of wavelength and d is the film thickness [54].

The UV-Vis spectroscopy for this project was performed with a Horiba QuantaMaster 8000 spectrofluorometer. The film thicknesses used in equation (10) were estimated using ellipsometry.

2.4.7 Photoluminescence (PL) & Time-Correlated Single Photon Counting (TCSPC)

PL involves shining light of a known wavelength onto a sample, for example a semiconductor, to induce excitation of electrons to a higher energy level, as the first step of a process to elucidate the optical properties of semiconductors or organic molecules. This excited state may decay rapidly, causing the sample to re-emit light in the form of a photon for each electron that falls back down, of energy equal to the energy difference between the initial and final energy levels of the electron. Often competing with this fluorescence process may be a number of non-radiative processes, such as thermalisation of an electron back down to a lower energy by energy dissipation through phonons. The emitted light is collected by a detector, and the PL intensity is noted across a range of wavelengths of interest that the sample may re-emit at [29]. The PL process thus allows for the determination of material bandgaps, evaluation of whether they are direct or indirect, the energies

at which materials emit and absorb, as well as information on band-tail states, defects and the impurity content of samples [29,55]. The use of PL that will be made here is for PL quenching tests to study the electron extraction capabilities of an ETL layer on top of which a light-absorbing perovskite layer was deposited. In this test, a single emission wavelength of the absorber material is focused on, and PL spectra are taken of the corresponding peak with different layers underneath, in this case ETLs. This yields a succession of peaks that overlap in x-coordinate but not in height, and a lower peak intensity suggests superior electron extraction capabilities by the ETL [7,8]. A greater peak intensity, on the other hand, is expected when electron-hole pairs remain in the perovskite to recombine and cause light re-emission (fluorescence), implying a failure on the part of the ETL to efficiently extract electrons from it [7].

TCSPC (or time-resolved PL) measures the decay curves of the emission of light from a sample. An excitation source sends a pulse of light towards a sample of interest, and individual photons re-emitted from the sample are counted in succession [56]. This allows statistical information to be gathered about the decay of light emission from the sample: the counted photons are categorised by the exact time interval after the light pulse is sent during which they were detected, producing a statistical distribution of photon counts over time intervals that can be hundredths of nanoseconds long. The result is a decay curve, showing how rapidly emission from a sample is attenuated following excitation [56]. Taking this a step further, the lifetimes of excited states following light absorption by a fluorescent sample (such as an electron-hole pair) can be estimated from fitting the decay curve to a mathematical relationship, usually a sum of exponential terms as shown in equation (11):

$$I(t) = A_1 e^{-t/\tau_1} + A_2 e^{-t/\tau_2} + \ldots + A_n e^{-t/\tau_n} \qquad (11)$$

where *I(t)* is the intensity of the light re-emitted by the sample as a function of time, and *A* and τ are amplitudes and lifetimes to be fitted [56]. The value of *n* will match the number of processes contributing to the lifetime observed, such as charge carrier extraction or electron-hole pair recombination, so that a lifetime can in theory be attributed to each process [7,56,57].

To produce the ETLs for both the PL quenching and TCSPC measurements, SALD was used, with the exception of the TiO_2 films which were spin-coated. A 1.5 x 1.5 cm ITO-coated glass substrate was used, and a 0.1 M precursor solution was prepared by mixing titanium diisopropoxide and 1-butanol in a 2:41 ratio by volume. The resulting mix was filtered with a 0.45 μm PTFE filter, before pipetting 50 μL of it onto the substrate and spin coating at 4000 rpm for 10 secs. The sample was then dried at 125°C for 5 min. This spin coating and drying was repeated twice more for three layers in total to produce a ~50 nm-thick film. To top it off, the TiO_2 was heat treated for half an hour at 450°C to consolidate the layers [40]. All other ETLs were deposited onto glass that was not coated in ITO.

A film of lead halide perovskite was then applied atop all of the ETLs before the quenching and TCSPC tests, for which the same samples were used. The ETL-coated samples were first sonicated in isopropanol for 7 min then blow dried in air, before being ozone-cleaned for 30 min. Ozone cleaning was found to be crucial in order to deposit a uniform film on top of a ZnO or ZTO ETL, without which the solvents and surface repel each other. This is likely due to the ozone increasing the hydrophilic character of the oxide, and it removes radicals from the ETL surface that can degrade the perovskite more rapidly. To produce the perovskite layers in a glovebox, iodides of caesium (0.0987 M), FA^+ (1.25 M) and lead (1.401 M) were dissolved into dimethylformamide solvent (DMF), and guanidinium iodide (0.0833 M) was dissolved into dimethyl sulfoxide (DMSO). These two solutions were filtered and mixed in a 76%:24% ratio by volume of

DMF:DMSO solutions. A 50-50 mix of chloroform and chlorobenzene was used as anti-solvent. 50 μL of the perovskite precursor solution was then spin coated at 1000 rpm for 10 secs, then at 6000 rpm for 20 secs. In the last 5 seconds 300 μL of anti-solvent was pipetted onto each sample. Finally, the perovskite films were annealed on a hot plate at 90°C for 25 min.

The excitation of the samples during the PL quenching tests was done with 680 nm radiation, for TCSPC the source wavelength was 350 nm and the test was stopped when the highest count number reached 1000. Both of these tests were performed in the same apparatus as the UV-Vis spectroscopy: a Horiba QuantaMaster 8000 spectrofluorometer. For both tests, 825 nm was the wavelength scanned for emission from the samples (although for PL quenching a spectrum of wavelengths encompassing the 825 nm peak was scanned: 815-835 nm).

2.4.8 Drive-Level Capacitance Profiling (DLCP)

DLCP is a variation of capacitance-voltage (C-V) profiling, the latter involving measuring the junction capacitance while altering an applied DC bias [58]. DLCP can provide information on the charge carrier density of a semiconducting thin film (and estimate it much more accurately than C-V profiling) along with the density of its carrier-trapping defects [41,58,59]. DLCP is better suited to the study of thin films that have a high concentration of defect states providing energy levels within the bandgap, as C-V profiling tends to overestimate their carrier density. This is the case for polycrystalline and amorphous nanofilms [41,58]. To carry out DLCP, an impedance analyser applies a changing DC bias to counteract the magnitude of the AC bias, ensuring a constant maximum voltage ($V_{max} = V_{DC} + V_{AC}$) [41]. An example of this is shown in Figure 9, as was used here. Keeping V_{max} at a set value is important to ensure that the film is being examined at the same depth during a measurement, as increasing the total potential difference applied will cause the film to be probed at a different depth; further away from the Schottky junction [41,58].

The AC and DC biases are varied in tandem over a range of frequencies, to yield a graph of capacitance against AC bias which is to be fitted (usually with a second order polynomial). This is repeated at each frequency in the chosen range [41].

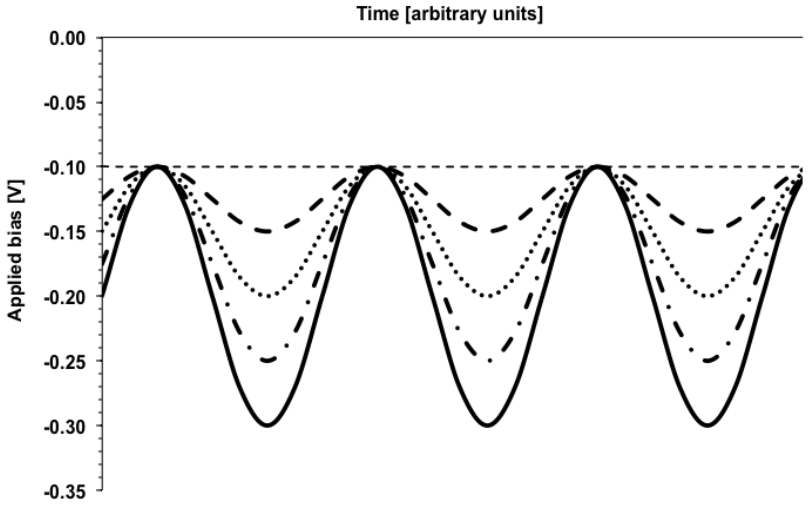

Figure 9: DC bias variation across a sample to maintain the V_{max} at a given value [41]

In DLCP, a relatively large AC potential difference is applied across a material to bring about a non-linear dQ/dV response, such that the non-linear terms in equation (12) become important, where Q is the charge.

$$\frac{dQ}{dV} = C_0 + C_1(dV) + C_2(dV)^2 + \cdots \qquad (12)$$

The '*C*' coefficients are functions of electrical and physical parameters of the tests. Their values must be determined (from fitting the capacitance function) in order to calculate the charge carrier density (*N*) as a function of distance from the junction (X_e) using equations (13) and (14) [41]

$$N = \frac{|p_e|}{q} = -\frac{C_0^3}{2q\epsilon A^2 C_1} \quad \& \quad x_e = \frac{\epsilon A}{C_0} \qquad (13)\ \&\ (14)$$

where q is the elementary charge, A is the contact's area, $\mathcal{E}$ is the permittivity of the medium, and p_e is the charge density. A graph of N against X_e is useful for determining several different parameters of the semiconducting nanofilms under scrutiny. DLCP works by having the AC bias oscillated back and forth at an increasing frequency, and the greater the magnitude of the applied bias, the further away from the Schottky junction the carrier depletion region of the semiconducting film will extend. Therefore, oscillating the bias will produce a layer of material for which majority carriers should repeatedly be removed from and re-enter, if given sufficient time to do so. Consequently, energy levels in the band gap (corresponding largely to the existence of defects) will not have enough time to accept or release their trapped carriers according to what the bias commands at higher frequencies in that layer, and in that layer charge densities remain the same during the bias application cycle [58]. So, at lower frequencies, the N value represents the maximum density of states able to respond to the oscillating voltage: both deep and shallow bandgap states. At higher frequencies however, the value of N will be smaller and nears the free carrier density, as only these carriers and not the trapped ones are able to keep up with the rapid perturbation in bias. The density of defects is calculated as the difference between the N values at the high and low frequencies [41,58].

The ZTO films for DLCP measurements were deposited by SALD on top of ITO-coated 1.5 x 1.5 cm glass substrates, with one of the corners taped to leave some of the ITO film exposed. The thickness of the ITO film was 300 nm. To carry out the measurements, 75 nm-thick Al electrodes approximately 2 x 2 mm were first thermally evaporated onto the substrates; 4 in a square atop the ZTO films to allow for more data to be taken so a representative average of properties across the films could be taken, and one atop the underlying ITO at the corner of the samples so that it made no contact with the ZTO. Measurements across different AC and DC bias combinations were then

taken at 10 different frequencies between 40 Hz and 1 MHz, and this data fitted to a Randles cell consisting of a resistor and a capacitor in parallel (to model the oxide film) in series with another resistor representing the series resistance of the experimental set-up (Figure 10). The capacitance values were extracted from this fitting. The measurements were carried out using a Gamry Instruments Interface 1000E Potentiostat/Galvanostat/ZRA, and fitting was done using the Gamry Echem Analyst software.

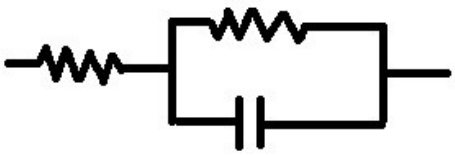

Figure 10: Schematic of the Randles cell used to fit the DLCP data

2.4.9 Van der Pauw Four-Point Probe Resistivity

The van der Pauw method allows measurement of the electrical resistivity of thin films through first determining the sheet resistance and multiplying it by the thickness of the film which must be known [60,61]. The method can be understood as a configuration of the four-point probe technique that is more appropriate for films that do not have a simple or regular shape. In it, four electrical contacts (which should be ohmic) are placed on the outside of the film, at arbitrary positions [60,61]. Provided that the contacts are attached onto the outer edge of the sample, that they are of sufficiently small area relative to that of the film, that the sample has uniform thickness and composition, and that the film being measured is continuous in that it does not have holes, the method can provide accurate resistivity values [60,61]. The measurements themselves are carried out as follows, assuming the sample is somewhat square. A DC current is made to flow between two of the contacts along one edge, and the DC potential difference between the other two contacts

on the opposite edge is measured. By dividing the voltage by the current, the resistance in one direction, say vertical, can be obtained (Ohm's law). By repeating this measurement in the other direction, a similar horizontal resistance can be calculated. The van der Pauw formula (equation (15)) can then be solved to yield the sheet resistance R_S:

$$e^{-\pi Rv/Rs} + e^{-\pi Rh/Rs} = 1 \qquad (15)$$

where Rv and Rh are the vertical and horizontal resistances [61]. The van der Pauw method for resistivity can be taken further to give more accurate results, thanks to the reciprocity theorem: $R_{AB,CD} = R_{CD,AB}$, where $R_{AB,CD}$ indicates that the voltage was measured between electrodes C and D while a current was applied between A and B (see Figure 11).

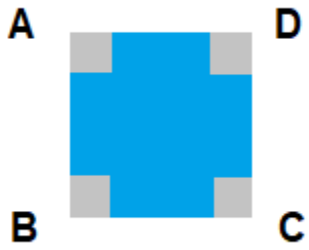

Figure 11: Contact reference positions for a square sample

Rv is then more accurately represented by a mean average of both vertical resistances, and the same goes for Rh (equations (16) and (17)) [61].

$$Rv = \frac{R_{AB,CD}+R_{CD,AB}}{2} \quad \& \quad Rh = \frac{R_{BC,DA}+R_{DA,BC}}{2} \qquad (16)\ \&\ (17)$$

Equation (15) can then be used again with these more accurate resistance values to obtain a new R_S. On top of these 'reciprocal measurements', an even further improvement to accuracy can be made thanks to 'reversed polarity measurements'. For this final layer of improvements, the voltage measurements are repeated with the polarities switched (electrodes inverted) for both the current

source and voltage measurement when calculating each of the resistances, so that *Rv* and *Rh* are now produced from a mean average of 4 values: the ones from the numerators of equations (16) and (17), as well as those same ones with their polarities reversed [61].

The samples for the van der Pauw resistivity measurements were ~1 x 1 cm glass substrates cut from a larger one on which ZTO had been deposited with SALD. Thermal evaporation was used once again to evaporate 75 nm-thick Al electrodes 2 x 2 mm on each of the 4 corners of the samples. The current was applied and the potential difference measured across the electrodes using a Keithley SourceMeter 2400.

CHAPTER 3: CHARACTERISATION OF NANOFILM COMPOSITION & COMPOSITION-DEPENDANT PROPERTIES

3.1 Relationship Between Deposition Conditions and ZTO Composition

One way to express the composition of a ZTO film is with the tin content fraction, or the ratio of the atom% concentration of tin atoms against those of all metal atoms in the film [29]. Quantitatively, this can be expressed as shown in equation (18).

$$Sn\ content = \frac{[Sn]}{[Sn]+[Zn]} \qquad (18)$$

The Sn content of the ZTO films was determined using XPS spectra, on which analysis was carried out using CasaXPS software to yield relative atom% concentrations of each element present in the films. This allowed for calculation of the tin content using only XPS measurements. To vary the Sn content of the ZTO films produced, the flow rates through each of the Sn and Zn precursor bubblers were altered. A comparison of how the different deposition conditions affected the Sn content of the films is displayed in Table 1.

Table 1: Differences in Deposition Parameters vs. Sn Content of ZTO Films

Film ID	Zn Bubbler Flow [sccm]	Sn Bubbler Flow [sccm]	Sn Content [%]
Set 1, Film 1	25	300	32
Set 1, Film 2	21		30
Set 1, Film 3	17		73
Set 1, Film 4	13		78
Set 1, Film 5	9		79
Set 1, Film 6	5		97
Set 2, Film 1	***50***	***225***	***57***
Set 2, Film 2	***40***		***57***
Set 2, Film 3	***30***		***54***
Set 2, Film 4	***20***		***43***
Set 2, Film 5	***10***		***59***
Set 3, Film 1	50	165	38
Set 3, Film 2	45		0
Set 3, Film 3	40		33
Set 3, Film 4	35		31
Set 3, Film 5	30		31
Set 3, Film 6	25		31
Set 4, Film 1	***50***	***265***	***33***
Set 4, Film 2	***45***		***34***
Set 4, Film 3	***40***		***31***
Set 4, Film 4	***35***		***1***
Set 4, Film 5	***30***		***31***
Set 4, Film 6	***25***		***31***
Grad. Set, Point 1*	40	≤75*	33
Grad. Set, Point 2	40		0
Grad. Set, Point 3	40		33
Grad. Set, Point 4	40		28
Set 5, Film 1	***25***	***300***	***35***
Set 5, Film 2	***17***		***71***
Set 6, Film 1	21	225	30
Set 6, Film 2	13		37

*Refers or relates to a gradient deposition which will be explained later.

It should be emphasised that all depositions in Table 1 were done under the same conditions, save for the flow rates through the precursor bubblers detailed in it. The only other deposition conditions

that would have varied would be minute differences in the gap width between the substrate and reactor head, and the number of oscillations across depositions, but these are unlikely to affect Sn content significantly. Other than those, Table 1 can be assumed to be a fair comparison across near-identical deposition conditions.

It is seen in Table 1 that a large range of Sn contents, from 0-97%, were observed in the ZTO films. As will be explained however, the contents of about 0% are likely not representative of the true compositions, and so to say that a range of 30-97% for the Sn contents was observed is more accurate. The way in which the compositions of the films varied with bubbler flow rates was somewhat unexpected, and a search for similar studies revealed that this may be the first time that such a broad range of Sn contents was achieved for ZTO films deposited by SALD. SALD has been used before to produce ZTO films with Sn contents between 0 and 26% [29], while conventional ALD has achieved the entire range of tin contents: from 0 to 100% [30,62]. It would have been logical to presume that the greater the flow rate through the Sn precursor bubbler, the more Sn-rich the ZTO film produced. The trend observed was not quite so simple, and this expected trend between Sn bubbler flow rate and Sn content was only seen below a threshold flow rate of about 21 sccm through the DEZ bubbler. Only when the DEZ bubbler flow rate was below this threshold value (such as for Set 1 Films 3-6, Set 2 Films 4-5, Set 5 Film 2, and Set 6 Film 2) do we see Sn contents that deviate significantly from the standard value of ~30% seen in most of the other rows (except for Set 2 for which this standard value was ~55%). When below that threshold value of ~21 sccm through the DEZ bubbler, decreasing the DEZ flow rate decreases the Zn content in the films, as might be expected. These two deposition regimes above and below the threshold flow rate are shown graphically in Figure 13. Regardless of whether the flow rate through the Sn bubbler was 75 sccm, 300 or any value in between, when the flow through the DEZ bubbler

was above the threshold value of ~21 sccm, varying the flow through the Zn bubbler did not alter the composition of the films across a deposition set. Perhaps more surprisingly, the Sn content always seemed to settle to about 30% across all sets despite varying the bubbler flow rates throughout the sets (except for Set 2 where the Sn content settled to ~55%). The only depositions that produced sets of nanofilms in which the composition could be controlled (at least to an extent) was when the flow through the DEZ bubbler was taken below ~21 sccm (i.e. Sets 1, 5, and 6). Only then did the Sn content deviate from ~30% (or ~55% for set 2); when in these 'low Zn' conditions, ZTO nanofilms with compositions anywhere between 30% and ~100% Sn content were achieved.

There appears to be the odd deposition for which Sn incorporation into the film failed almost entirely. This is seen for example in the cases of Set 3 Film 2 and Set 4 Film 4, and does not make much sense. One explanation could be that if a sample from the edge of a substrate was selected for XPS, one with a film from an area that was not directly below the reactor head during deposition but just beside it, a ZnO sample could have been given for XPS analysis. This is possible if ZnO was more prone to CVD deposition, causing some to deposit outside of the area strictly below the reactor head whereas SnO_2 deposition could have been purely ALD-like and deposited only immediately underneath the reactor. Indeed, some deposition was frequently observed outside the zone that would have been just under the reactor head on the substrate.

'Grad. Set' in Table 1 refers to a gradient deposition set. A colleague developed a gradient reactor head in which one of the slits for the metal precursor delivers the dose of the reactant in an approximately linearly increasing fashion along the length of an SALD nanofilm, as illustrated in Figure 12. The effectiveness has been demonstrated to produce thickness gradients across a nanofilm [43], but since the reactor heads designed contain a standard non-gradient slit as well,

the gradient reactor was tested to try to produce a composition gradient across the films, with TDMASn blown through the gradient slit and DEZ through the other, allowing for making more ZTO compositions with fewer depositions. This is what is meant by the 'less than or equal to' sign in Table 1: there was 75 sccm of N_2 flowing through the Sn bubbler, leading to approximately that flow rate on one side of the film, which decreased linearly towards the other side. Points 1-4 in Table 1 correspond to 4 equidistant spots of XPS measurement in a line along the expected gradient, with point 4 supposedly receiving the greatest TDMASn dose. Unfortunately, the difference between the low Zn and higher Zn conditions had not been realised by the time gradient depositions were attempted, and so since a flow rate of DEZ corresponding to 40 sccm through the bubbler was supplied uniformly to the film, the composition gradient hoped for was not seen. In hindsight, retrying this with less than 21 sccm through the DEZ bubbler provides an interesting opportunity for future work as it is probable that this will produce a successful ZTO composition gradient.

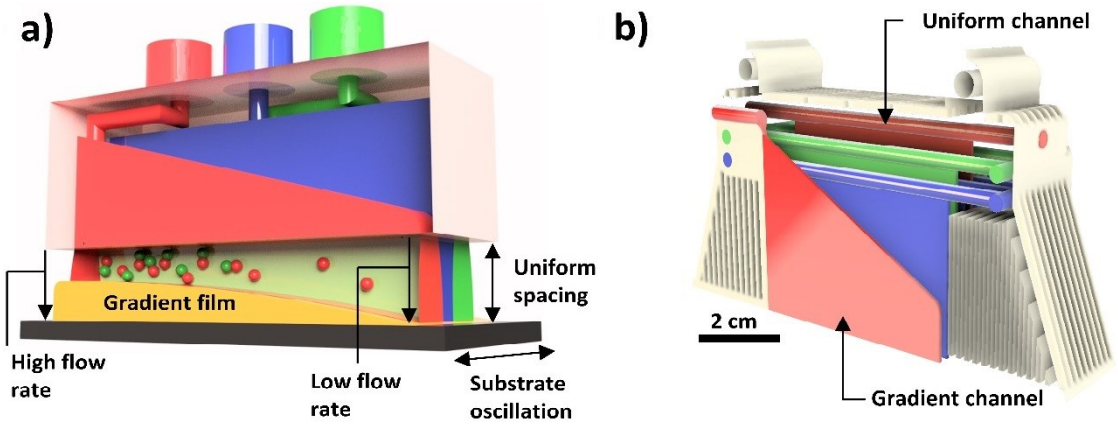

Figure 12: a) Operating principle of the gradient channel & b) Reactor head with both a uniform and gradient slit incorporated into it [43].

A statement can be made about reproducibility of Sn contents at similar bubbler flow rates in low Zn conditions, providing some indication that the technique is reliable for controlling the

composition of ZTO, although there are few rows from Table 1 to speak to that effect. Set 1 Film 3 and Set 5 Film 2 have identical deposition conditions including the bubbler flow rates, and their Sn contents were very similar: 73% and 71%. There is also the question of the flow rates that should be used if one wants to target a specific new ZTO composition for a film. To that end, Figure 13 should provide some insight.

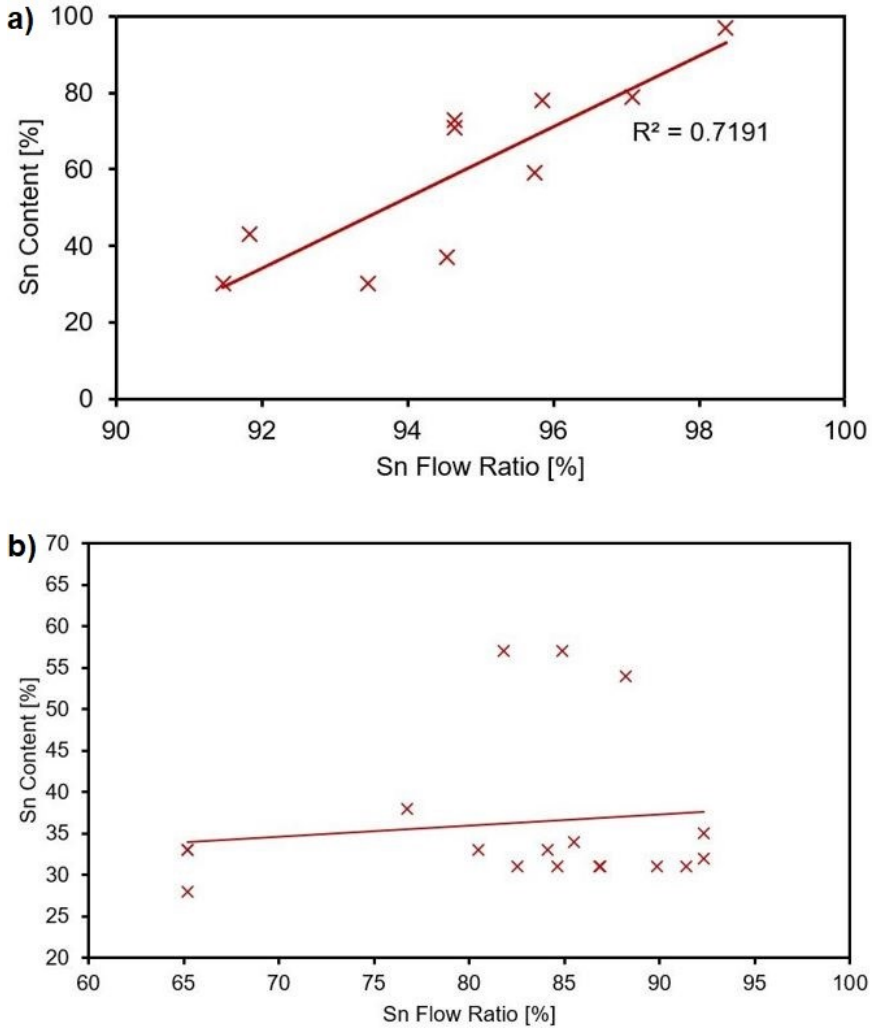

Figure 13: Sn content against % flow ratio through the Sn bubbler over the sum through both bubblers for a) low Zn conditions (≤21 sccm through the DEZ bubbler) & b) higher Zn conditions (>21 sccm through the DEZ bubbler)

Although more data would need to be collected for a more accurate relationship, the Sn content in low Zn flow conditions seems fairly well correlated to the proportion of the total bubbler flow passing through the tin bubbler. This points to predictability as well as repeatability of composition control with this ZTO SALD technique being possible. Some deviation from the linear relationship is observed with points lying some distance away from the trendline, casting some doubt as to the capabilities of the method for pinpoint composition control. However, as will be detailed in section 3.2, having the DEZ bubbler flow fixed and varying the TDMASn bubbler flow may not be exactly equivalent to the reverse. For instance, comparing Set 1 Film 4 and Set 6 Film 2, we see that increasing the Sn bubbler flow rate by 75 sccm boosts the Sn content by 41%, for the same DEZ flow rate. Conversely, for the same TDMASn flow rate, a 24% boost in Sn content is seen when decreasing the DEZ flow rate by just 12 sccm (Set 1 Films 3 and 6). Figure 13 comprises of points from both of these alternatives (represented by the choice of bubbler flow rate to keep fixed), and it may be an oversimplification to plot these both on the same graph. One graph for each could allow for stronger correlations and so increased predictability of the deposition parameters' effect on composition.

3.2 Theory to Explain the Effect of Deposition Parameters on Composition

The problem of explaining the observations from section 3.1 is one for which there may be very little precedent. Although some studies that relate to thermodynamics or kinetics of ZTO deposition by ALD have been carried out before, they may not reflect the conditions used in the experiments done here. Only one report of ZTO deposition by SALD rather than ALD has been found, and it was by co-injection SALD in which the surface would have been exposed to both precursors at once and there would have been competition between DEZ and TDMASn for surface reaction sites [29]. The reaction conditions used here are quite different, as the Sn and Zn

precursors were delivered by separate channels. Thus, a theory will be proposed in this section for SALD deposition of ZTO using different metal channels for the precursors, in an attempt to shed light on how film composition can be controlled by this method.

To help with this, the main observations from section 3.1 will be summarised below. They will also be assumed to consistently hold true in order to elucidate the theory.

- Obs. 1) When in higher Zn conditions (>21 sccm through DEZ bubbler), the flow through the TDMASn and DEZ bubblers are irrelevant in affecting the final composition (in the ranges studied) and the Sn content settles to ~30%.
- Obs. 2) When in low Zn conditions (<21 sccm through the DEZ bubbler), decreasing the DEZ flow rate with a fixed TDMASn flow rate increases the Sn content of the ZTO.
- Obs. 3) When in low Zn conditions the TDMASn flow rate does have an effect, with a higher amount leading to a greater Sn content for a fixed DEZ flow rate.

It will also be useful to consider Figure 7 once again, which reminds us that the sequence of exposure of the film surface to the reactants was: TDMASn, O_3, DEZ, O_3, TDMASn, and repeat. With this in mind, the 3 observations can be explained as follows.

When in higher Zn conditions, the amount of DEZ blown out from its reactor head slit is sufficient to saturate the overwhelming majority of the reaction sites it is exposed to, leaving the surface covered either in -Zn-OH or rather the more likely -Zn-O* sites which may be more common following exposure to ozone. When depositing metal oxides by ALD, O_3 reacts by generating O* radicals on the oxide film surface [44]. Exposure of this radical-terminated surface to TDMASn then takes place. Since a broad range of TDMASn bubbler flow rates have been investigated without causing a change in the Sn content when in higher Zn conditions, then logically there must

be a factor dictating a maximum amount of TDMASn that can react with the radical-terminated surface. The key to explaining the persistent settling to a 30% Sn content lies in this saturation behaviour, and observation 1 can indeed be explained by both precursors being at flow conditions causing saturation of the surfaces (reaction sites) exposed to them.

Past studies can shed some light on why the amount of TDMASn that reacts with the surface saturates. DEZ has 2 organic ligands that are ideally removed following ALD reactions, and TDMASn has 4 such ligands which it can use to react. For ALD reactions using water, most of the DEZ molecules react with the nanofilm surface by losing one ligand, leaving the other to react and become a hydroxyl group after the next water step [38,63]. This causes no overall change in the number of reaction sites when comparing the 'before' and 'after' states for the DEZ exposure step. The Sn precursor molecule, however, can bond to an -OH-terminated surface using 'n' of its ligands, where n can be 1-4 in theory, but 4 is geometrically very unlikely in practice. For ALD depositions with water as the oxidant it has been determined that n=2.5-3 most commonly [38]. Figure 4 in section 1.6 shows the ALD reaction between TDMASn and H_2O in the case where n=2. This average value of n also accounts for cases where only one ligand may react with the surface, which can happen for example due to competition between tin precursor molecules for surface groups to react with, forcing molecules to react using 1 ligand when reacting with 2 or 3 of them has been calculated to be thermodynamically more favourable on a crystalline -Zn-OH surface [38]. Since n is on average larger than 2, it translates into a decrease in the number of reaction sites following TDMASn exposure in an ALD system compared to prior to it [38]. If n=3, a tin precursor molecule consumes 3 hydroxyl reaction sites to only produce one for the next layer with its last unreacted ligand. Looking back at Figure 4 but imagining 3 DMA ligands reacting with the surface instead of 2 may help to picture this. At least for reactions using water, this reaction site density

change effect plays a major role in ALD growth of ZTO, reducing the ZnO growth rate atop an SnO_2 layer compared to what would be the growth per cycle (GPC) of pure ZnO [34,38]. This decreased growth rate caused by taking up of multiple hydroxyl sites by TDMASn was put forward without accounting for the process kinetics or the surface's saturation limit during a deposition by ALD [38,63].

This effect could account for the saturation in Sn content from observation 1. If n=3, then on average about a third as many Sn precursor molecules should become incorporated into the film as DEZ ones in the previous layer. The Sn content would then be roughly 25%. If n=2, the content would be 33%, and the pattern may repeat as O_3 exposure after the TDMASn would produce 2 new O*-terminated reaction sites from one TDMASn molecule. This is shown in Figure 4 for the reaction with water instead of ozone. This way, Zn and Sn precursor molecules would keep reacting and becoming incorporated into the film in a 2:1 ratio. The 30% Sn content observed may imply that n is between 2 and 3 for ozone-grown ZTO at this temperature. Again, there are differences between the deposition/calculation parameters of the studies cited and those used here. That said, the ~30% Sn content value has occurred too often to be a coincidence, and the fact that this number is similar to what the ligand reaction theory would predict implies that the principal factor to explain this saturation behaviour has been correctly identified. Another factor that might play a role in explaining the maximum Sn content incorporated into ZTO is the availability of ozone molecules. The ALD growth rate of both ZnO and ZTO is very sensitive to the dose of O_3 supplied to the surface [44]. If the ozone dose, a fixed parameter across depositions, was insufficient to react with all of the ligands of the growth surface during exposure, it could explain why only as many TDMASn molecules would become incorporated into the film as the ozone dose would allow. This however appears unlikely to be the case when reminded that the balance

gas coming out of the ozone slits of the reactor head was mostly oxygen, which the precursors would also have been oxidised by. Thus the saturation behaviour would not have been oxidant-controlled, and further evidence to support this will be given later.

Once low Zn conditions are used, the amount of DEZ reaching the surface is no longer sufficient to saturate all reaction sites. Assuming an ALD-type reaction, immediately prior to a TDMASn exposure step, there are both -Zn-O* sites as well as -Sn-O* ones from the last TDMASn step that did not react with a DEZ molecule. Not only is there less Zn incorporated into the film simply because not as much DEZ reacted as could have if more had been supplied, but the TDMASn is now exposed to a surface that more closely resembles ZTO, with -Sn-O* sites left over, rather than a surface of almost only Zn-oxygen radicals. Reacting to form amorphous SnO_2, or more of a material identical to that of the existing growth surface, may be more thermodynamically favourable for the TDMASn. It may have a greater affinity for a like surface. Observation 2 is now explained quite straightforwardly.

Observation 3 states that in low Zn conditions the TDMASn amount has an effect, whereas it did not at higher Zn conditions. It should be noted that this observation is only born from comparing two rows of Table 1 (Set 1 Film 4 and Set 6 Film 2), and so there is less confidence in it holding true as it was not tested extensively. This theory of explaining the control over ZTO composition with SALD already provides a means of depositing a broad range of ZTO compositions even if observation 3 does not hold. But if it is to be explained, it is logical to start with the fact that even at high flow rates through the TDMASn bubbler, the composition still seems to be TDMASn-controlled (all other parameters remaining equal), whereas it was not at higher Zn conditions. This further supports the prior claim that the Sn content was not limited by the oxidant availability, or observation 3 would not have held true. Several factors can explain why a greater amount of Sn

precursor can react in low Zn conditions than could before. Firstly, since the DEZ is now no longer saturating the surface sites, the conditions may be breaking away from more monolayer-by-monolayer deposition, with zinc atoms being added in some sites but not others. This may mean a greater number of reaction sites for TDMASn, with sites along different 'layers' now being available on this rougher growth surface, atomically speaking. How having the same number of sites spread over different layers could lead to more TDMASn becoming part of the film is illustrated in Figure 14. The number of Sn precursor ligands that react per molecule may be different on flat and rougher surfaces. Another factor could be the creation of additional reaction sites through the removal of more organic ligands from the chemisorbed molecules. It was mentioned that not all of the potential reaction sites on the chemisorbed tin precursor molecules would react during a DEZ exposure step in low Zn conditions due to the lack of DEZ availability. This means that some TDMASn molecules that still have ligands available to react with would be exposed to more ozone steps before reacting, allowing for the reaction of a greater proportion of ligands into O* radicals, in case a smaller number of ozone passes did not fully remove them. This may lead to a more reactive growth surface inviting more TDMASn to become incorporated into the ZTO film and react at low Zn conditions. The final observation would then be explained.

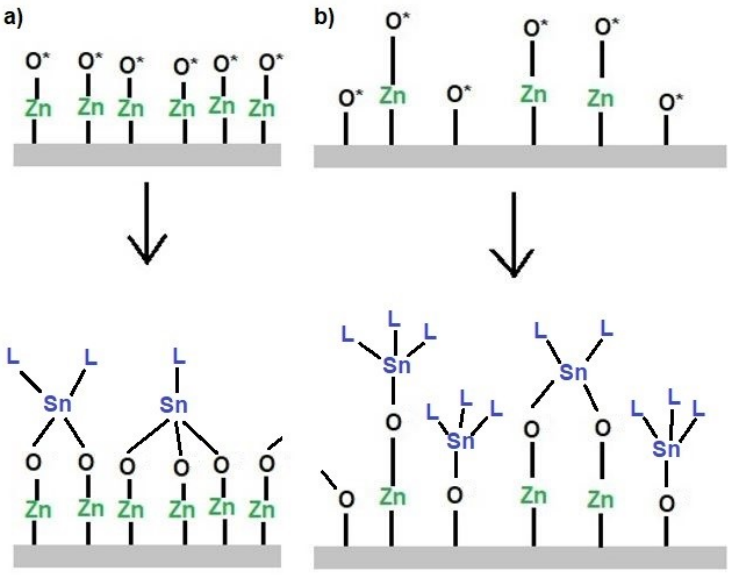

Figure 14: Possible SALD reaction of ZTO immediately before and after exposure to TDMASn for a) higher Zn conditions and b) low Zn conditions with a rougher growth surface. DMA ligands are abbreviated as 'L'. 'n' being estimated as 2.5-3 was for ALD or monolayer-by-monolayer growth [38]. It is possible that a rougher growth surface invites n to take on a smaller value.

One other element from past studies is worth mentioning - that the removal of precursor ligands from a growth surface can be less than perfect. It has been demonstrated that in the deposition of tin and zinc oxides with water by ALD the reactions were plagued by incomplete removal of ligands from the surface, including at temperatures as high as 150°C [34]. Even extended water pulses were not sufficient to fully remove the ligands from TDMASn [34]. Thus, one might think that there is a risk of the films deposited in this project to have had problems of purity and contain remaining ligands, a problem that may worsen at lower Sn contents since ligands were more effectively eliminated in SnO_2 deposition than in that of ZnO for the ALD reaction with water [34]. That said, ligand removal became more effective as the deposition temperature was increased, and at 200°C the TDMASn ligands are almost completely removed [34]. Ozone was also used instead of H_2O and it is a more powerful oxidising agent, and so the deposition temperature of 165°C and

the choice of oxidant would have favoured a more complete removal of the ligands for these ZTO films [44].

3.3 Growth per Cycle

The GPC of a material grown by ALD is the amount of thickness added to it per traditional ALD cycle, where such a cycle is the sequence of exposure to: the metal precursor, the purging gas, the oxidising agent, then the purging gas again. Since SALD involves back-and-forth oscillations of the substrate relative to the reactor head which provides a similar sequence of exposure, instead of just in the forward direction, there will be a conversion factor to apply to the growth per SALD oscillation and number of cycles to nucleation to convert to ALD cycle equivalents. If the reactor head has multiple metal precursor or oxidant slits, the conversion factor may be different as the substrate is exposed to a larger number of ALD-equivalent cycles per oscillation. What is meant by the number of cycles to nucleation is the number of cycles early in the deposition onto a fresh substrate (or onto a layer of a different material than the one you are currently depositing) before it can be claimed that a film exists or has nucleated. It can be seen as the number of cycles to produce the first material monolayer.

These parameters of interest were studied using ellipsometry to estimate the thickness of ZTO nanofilms grown with a different number of oscillations of the reactor head. To obtain a single thickness value for each nanofilm, 4 points on them were randomly chosen and their thicknesses measured, then a mean average using these points was calculated. The GPC and cycles to nucleation were studied for films with deposition conditions identical to those of Set 4 Film 3 from Table 1. The results are shown in Figure 15.

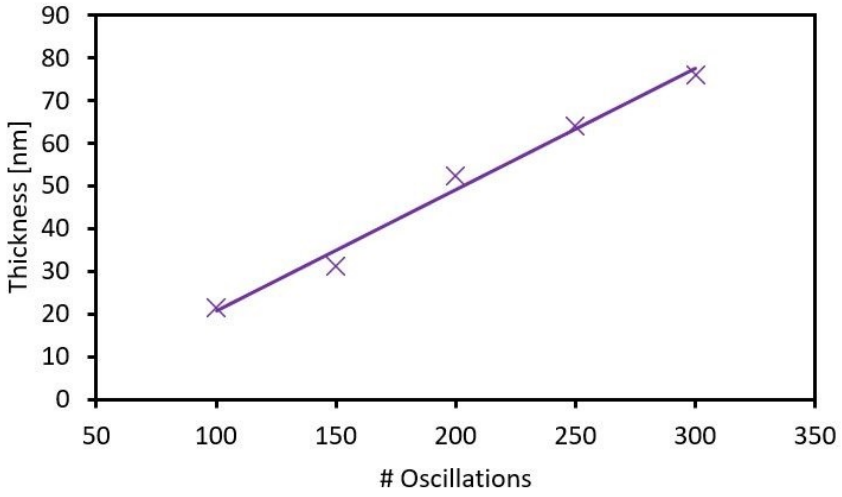

Figure 15: ZTO nanofilm thickness against number of SALD oscillations (deposition conditions: 40 sccm through the DEZ bubbler, 265 sccm through the TDMASn bubbler)

A linear trendline can be easily applied to the data in Figure 15. Judging from its gradient and from an extrapolation of the line towards the horizontal axis, the values of 0.28 nm/oscillation for the growth rate and 27 oscillations to nucleation are obtained. Accounting for the fact that one oscillation of our SALD reactor head is equivalent to four traditional ALD cycles, this yields values of 0.07 nm/cycle for the GPC and 108 cycles to nucleation.

Table 2 provides GPCs from other studies for similar oxide film growth at various temperatures and by similar deposition methods. It can be seen, despite a certain extent of variation in the different deposition conditions across the studies in Table 2, that deposition by SCVD boasts a GPC one whole order of magnitude greater than that of ALD and SALD, for which the GPCs are very similar for these oxides. For growth rates of ZnO at the same temperature, another group reported that deposition by SCVD benefited from a GPC that was one order of magnitude higher than the deposition rate by ALD, in agreement with Table 2 [10]. The GPC found here for ZTO

with an Sn content of 31% was 0.07 nm/cycle, both in solid agreement with the GPCs from Table 2 and suggesting a more ALD-like reaction mechanism as opposed to CVD-like.

Table 2: GPCs of ZTO and Similar Oxides across Different Deposition Techniques

Metal Oxide	Deposition Temp. [°C]	Deposition Method	GPC [nm/cycle]	Reference
SnO_2	80	SALD	0.15	[11]
SnO_2	120	ALD	0.11	[4]
SnO_2	150	SALD	0.11	[42]
ZnO	120	ALD	0.16	[4]
ZnO	150	S-CVD	~1	[43]
ZTO 40%*	120	ALD	0.04	[4]
ZTO 26%	225	SALD	0.02	[29]

*40% of the ALD cycles used Sn precursor rather than Zn precursor (Sn cycle fraction rather than an Sn content of 40%).

That said, declaring the ZTO deposition under these conditions to be more ALD-like may not be quite so straightforward. Figure 16 depicts 2D thickness maps for a selection of the SALD-deposited ZTO films. The 'fit_diff' parameter quantifies how well the fitted model echoes the ellipsometer measurements, and the target value for single layer sub-100 nm films should be about 0.001. All films below that thickness value had similar fit differences, implying a good confidence in the results obtained. The bandgap (E_g) values presented may not be very accurate however, as will be examined in greater detail in section 3.4. As can be seen from mapping the thicknesses over areas of about 4 x 4 cm, the uniformity can vary across a film and between the films - some films are largely uniform (Figure 16-a), but others are not (Figure 16-c). This implies local variations in the growth rates at different spots of a substrate, but uniform ALD-like deposition across the whole film would mean controlled monolayer-by-monolayer deposition everywhere,

and therefore more uniform thicknesses. Uniformity variations are a trait more reminiscent of CVD-like deposition modes.

Despite this, the claim will still be made that the deposition mode observed here for the ZTO films is much closer to ALD than to CVD, although it is most likely somewhere in between instead of exactly corresponding to monolayer-by-monolayer deposition. There is a clear difference between ALD-like and CVD-like GPCs, as seen in Table 2. The GPC of 0.07 nm/cycle calculated here is slightly higher than what was reported for ZTO ALD and SALD, but it is still far smaller than the 1 nm/cycle expected from a CVD-like deposition mode. If we consider the film from Figure 16-c, we can see the thickest areas were twice as thick as the thinnest ones, and so doubling or halving the calculated GPC may be appropriate. But even if the GPC in some areas was 0.14 nm/cycle, it is not on the order of magnitude of CVD GPCs. This was investigated further by calculating the GPCs for the thickest and thinnest areas of the films in Figure 16, assuming that the estimated 27 oscillations to nucleation were a constant for all films. The GPCs for the thickest areas of the films in Figures 16-a to 16-d were calculated to be 0.18, 0.25, 0.25 and 0.1 nm/cycle respectively. These being similar to the GPCs for deposition of the pure native oxides in Table 2 also points to more ALD-like growth being the favoured mechanism.

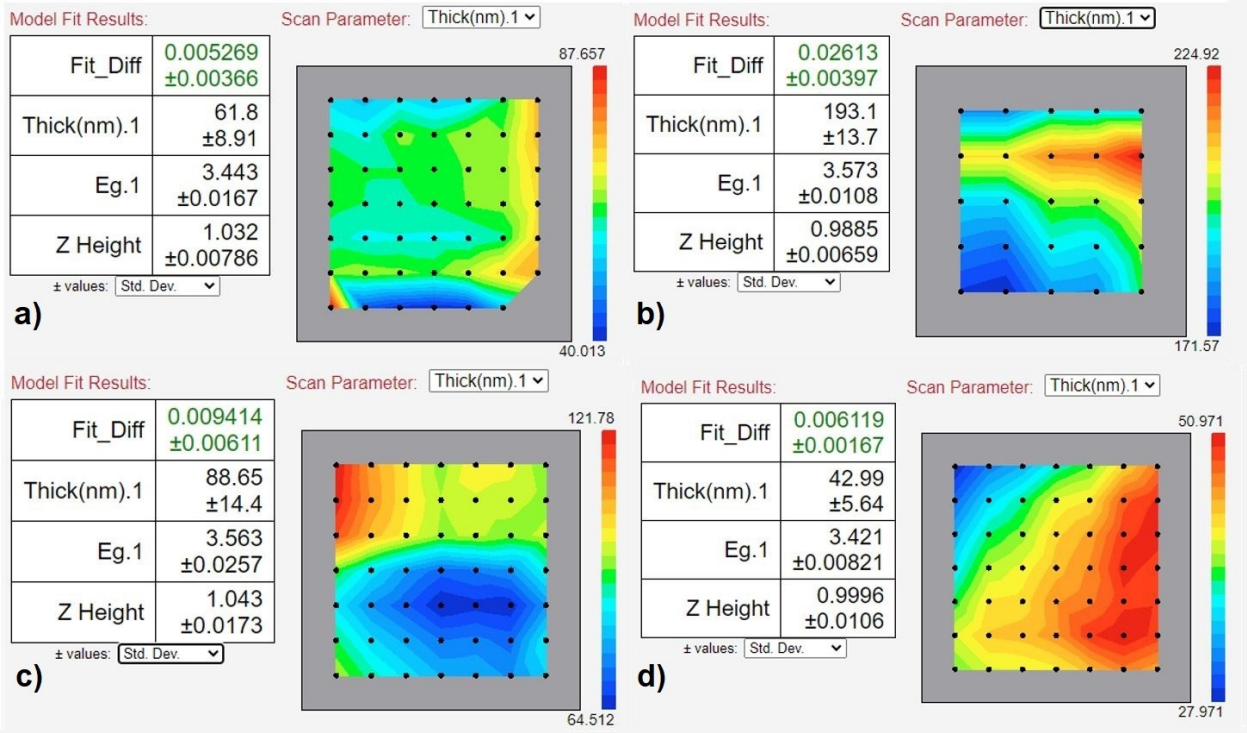

Figure 16: Ellipsometry-Obtained (Tauc-Lorentz Model) 2D Thickness Maps for an Area 4 x 4 cm on various ZTO Films, from a) a film for the GPC study, conditions were identical to Set 4 Film 3 (150 oscillations) b) Set 1 Film 5 (250 osc) c) Set 2 Film 2 (150 osc) d) Set 3 Film 1 (150 osc)

The lack of thickness uniformity in some films and the deviations from the more monolayer-by-monolayer deposition that the calculated GPC implies can be explained. Factors involved that may have contributed to less-than-ideal control of the reaction process may be difficulties in perfectly levelling the reactor head relative to the substrate stage, or the use of the exhaust channels seen in Figure 7 which was passive rather than with gas actively drawn out through them. Uneven precursor delivery along a slit or substrate, leading to sub-saturation growth conditions locally, could also have been a factor. This could have been seen for instance if the substrates had variations in their flatness. There were depositions in which the reactor head's bottom surface was not exactly parallel to the substrate, leading to uneven reactor-substrate spacing underneath the reactor. Since slit-to-substrate distance affects the degree of inter-mixing of the gases from the various slits and

therefore where the reaction lies on the ALD-CVD scale, a slit at one side of the head may have favoured an ALD-like reaction with more CVD character than one at the opposite side. This could have produced an overall effect comparable to ALD-like deposition with a less pronounced CVD-like layer to the reaction added to the ALD one. The fact that gas was not being actively drawn through the exhaust channels may also have led to some reactant stagnation inside these slits or some random turbulence to the flows, resulting in somewhat uneven film deposition in ways that cannot be easily predicted. An adequate exhaust drawing strength for reactant and nitrogen curtain gases, coupled with a superior reactor head levelling system, would likely have brought out a more uniform ALD-like deposition mode for the ZTO.

3.4 Optical Properties of ZTO

The question of bandgaps of metal oxide nanofilms is not always straightforward, and depending on the characteristics of a film it can exhibit a bandgap quite different from that expected of a bulk or polycrystalline film. For instance, SnO_2 has a direct bandgap of around 3.8 eV when polycrystalline, but its amorphous form often deposited by ALD can have one as low as about 2.4 eV, which may be due to oxygen atom deficiencies [30]. ZTO can exhibit both direct and indirect bandgaps. When it is microcrystalline its bandgap is direct, and indirect when amorphous [29]. This implies that the type of bandgap for ZTO can change with annealing temperature. It also suggests that ZTO undergoes a change in the type of bandgap as its composition changes, since for ALD/SALD films the material was found to undergo a microcrystalline-to-amorphous transition as the Sn content increased past 10-15% [4,29,62]. Since all films deposited here had Sn contents higher than 15%, they are expected to be amorphous [29,62] and the indirect bandgaps that will be reported are likely a better representation of the film properties than the direct ones, although both will be reported as is common in the literature [62].

As detailed in section 2.4.6, the bandgaps were obtained graphically, beginning with obtaining the absorption coefficient as a function of wavelength using an absorption spectrum, such as that shown in Figure 17.

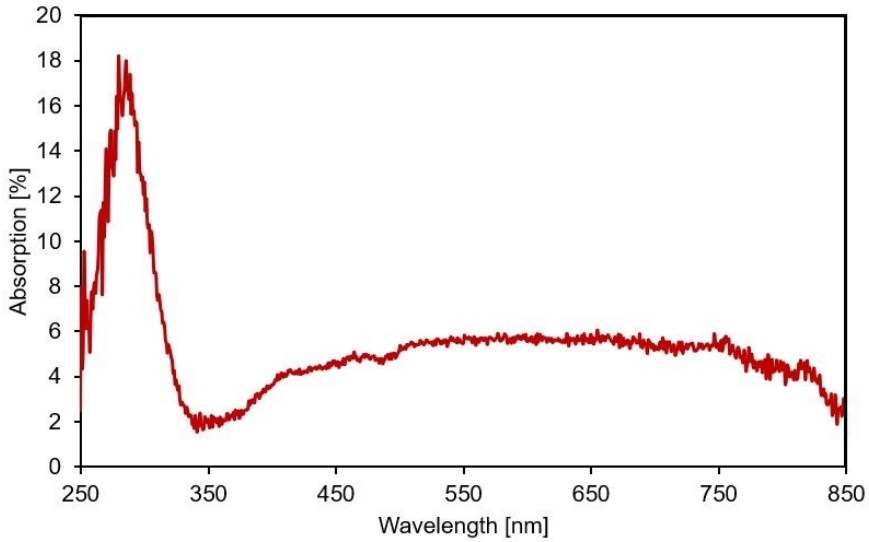

Figure 17: Absorption spectrum for a ZTO film with 57% Sn content

Once the absorption coefficient function was obtained, it was used to graph hv against $(\alpha hv)^{1/n}$ (see equation (9)). The whole exponent would have been equal to 2 for a direct bandgap and 0.5 for an indirect one, as shown in Figure 18 as an example. Equations fitted to the linear segments were then solved for y=0 to obtain the E_g values.

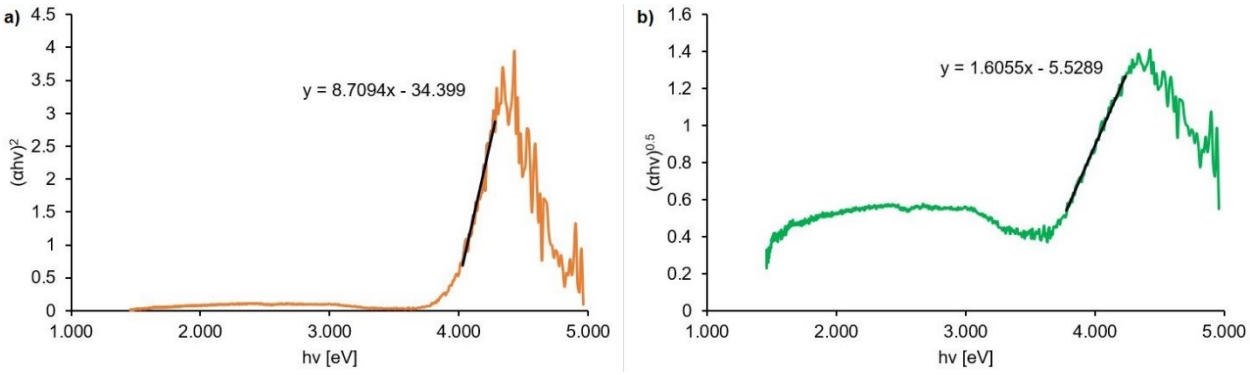

Figure 18: Tauc plots showing the linear fitted equations used to calculate the a) direct bandgap and b) indirect bandgap of a ZTO film with 57% Sn content

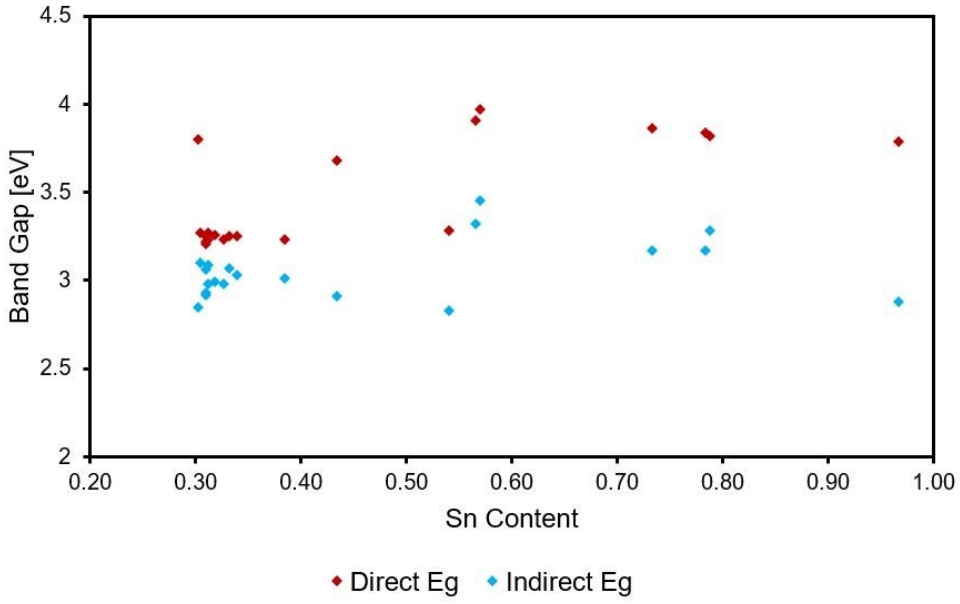

Figure 19: Tauc plot-derived direct & indirect band gaps for films in the 15-200 nm range

Figure 19 depicts the direct and indirect bandgaps obtained for most of the ZTO films deposited. Overall, a relatively modest change in the bandgaps is seen for as-deposited ZTO as a function of composition. If an indirect bandgap is assumed, then it is of about 3 eV at an Sn content of 30%, increases slightly to approach 3.5 eV at 50%, then decreases back down to 3 eV gradually as pure SnO_2 is approached. This indirect bandgap trend agrees quite well with previous reports on

SALD/ALD-deposited ZTO films for growth at similar temperatures, which reported similar observations [29,30,62]. At least for the composition range studied here, to say that ZTO exhibits an indirect bandgap of ~3-3.4 eV that shows somewhat limited variation with composition summarises the situation accurately, although this may change as the Sn content is taken below 15% due to increases in crystallinity and the accompanying switch over to a direct bandgap which can change value more abruptly with composition [29]. The situation may be different if very low Sn contents are introduced (Sn-doped ZnO), or if heat treatment of the ZTO is carried out after deposition, but the data from this project does not point to engineering the energy levels of a ZTO ETL (to better match them with a perovskite film) by varying the composition of an ALD/SALD ZTO film being straightforward. Although the range of indirect bandgap values seen (an ~0.4 eV difference between the highest and lowest values) can be of significant use in matching an ETL's CB and VB levels to an absorber's, the trend may not be clear or easily reproducible, as seen from the wide range of E_g values visible at ~55% Sn content. This presents challenges for using ZTO composition for E_g engineering. More testing with a greater number of samples would help to clarify the proposed trend in bandgap. Altering the deposition temperature to control the indirect bandgap of ZTO films of a similar composition may be a more fruitful strategy than compositional variation, as this affects the crystallite size leading to changes in quantum confinement effects on the bandgap [4].

To briefly consider the direct bandgaps: the values obtained here do not coincide as well with some of those reported in other studies, for which a trend with ZTO composition was observed. A somewhat linear increase from ~3.3-4.5 eV has been reported previously as the Sn content increases from 0 to 50%, before settling to 4 eV for a pure tin oxide film [62]. The bandgaps obtained here are about 0.5-1 eV below those values, and a correlation with ZTO content is less

apparent: two different direct bandgap values are sometimes visible at the same composition. At an Sn content of 55-57% for example, there is a data point showing a bandgap of 3.3 eV and two others closer to 3.9 eV. That said, these results are not as important as the ones of the indirect bandgap as they are not expected to represent the ZTO films as closely, and the claim has been made that morphological attributes of the films related to oxygen content or crystallite size can lower the bandgap quite drastically [4,30].

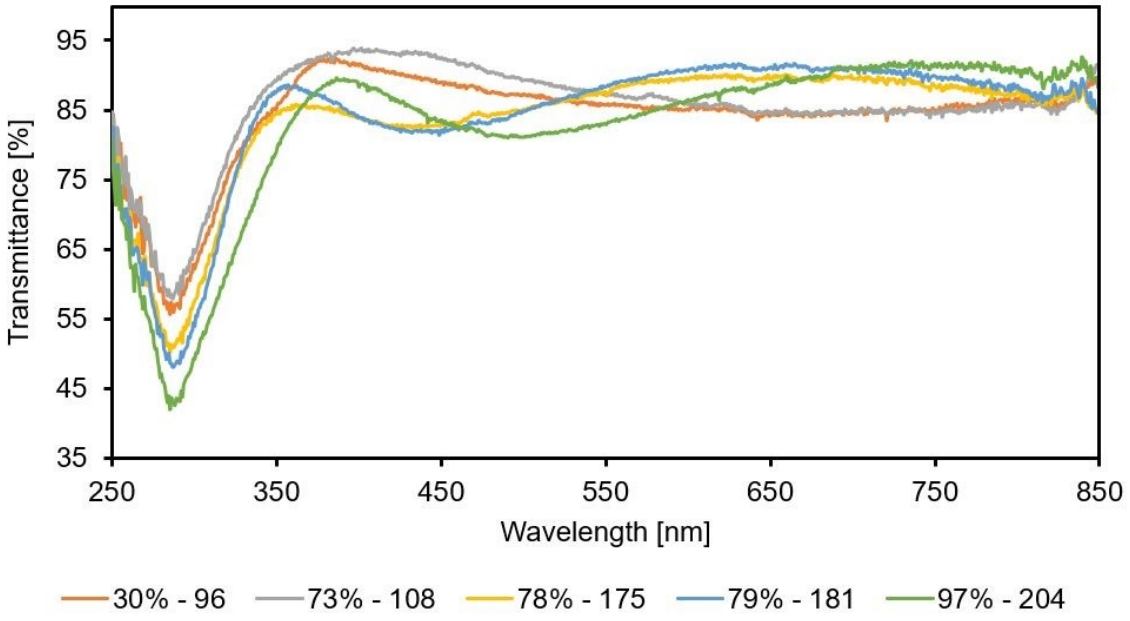

Figure 20: Transmittance spectra for films grown in low Zn conditions. Sn contents and thicknesses in nm shown in the legend.

The transmittance of the ZTO nanofilms was investigated with UV-Vis spectroscopy, with no sufficiently strong case made for any correlation between composition and transmittance. These curves were obtained from comparing two absorbance spectra for each film: one with the film plus the substrate and one on a blank glass substrate of the same thickness. The curves in Figures 20 and 21 are therefore attributed solely to the nanofilms, with any substrate effects having been

removed. Generally, two kinds of shapes were observed for the curves: ones where the lines began to dip at shorter wavelengths than 350 nm into a V-shape (Figure 20), and ones where the dipping began at longer wavelengths than 350 nm into a U-shape (Figure 21). The V-shapes were usually seen for low Zn deposition conditions and the U-shapes for higher Zn conditions, but this was not always so. A more consistent pattern would be in the fact that the V-shapes were for thicker films - ones thicker than about 80 nm. Thus, it could be that the shape differences are due to thin film interference effects in thicker nanofilms. The V-shaped transmittance spectra for thicker films show fluctuations in transmittance at wavelengths longer than 400 nm, which is not observed in the U-shaped spectra. For exposure to wavelengths longer than 350 nm, no consistent trend following either film composition or thickness can be observed, and the transmittance was almost always within the range of 80-95% for all films (and well above 80% at wavelengths longer than 550 nm). Thus, the ZTO films show an excellent transmittance over almost the entire visible light range. Where a trend could be observed was in the 250-350 nm range, but it was a correlation between the transmittance and the film thickness rather than the composition.

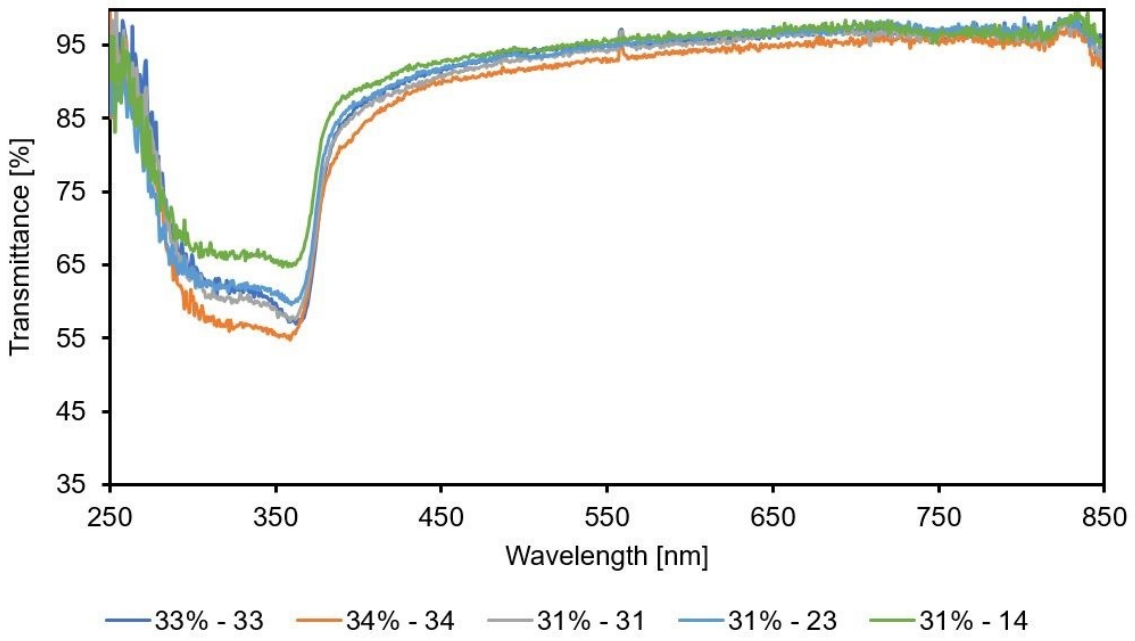

Figure 21: Transmittance spectra for films grown in higher Zn conditions. Sn contents and thicknesses in nm shown in the legend.

Optical data from ellipsometry is shown in Figure 22 for completeness. The refractive index at 633 nm (from a Cauchy model) and the bandgap (from a Tauc-Lorentz model) are graphed as a function of ZTO composition, although as has been explained a Cauchy model may not be the most accurate for ZTO and the bandgap values from ellipsometry are not expected to be as accurate as the ones extrapolated from Tauc plots. That said, the refractive indices determined from the Cauchy model fitting are well-matched with those of ZTO films from other studies, according to which n at 633 nm should be approximately 1.9-2.0 for the ZTO compositions studied in this project [62,64]. The numbers obtained here were rarely outside the range of about 1.8-2.0. The data in Figure 22 illustrates a clear lack of correlation between either the refractive index or the bandgap with the film composition over the range of x-values studied (as determined by ellipsometry).

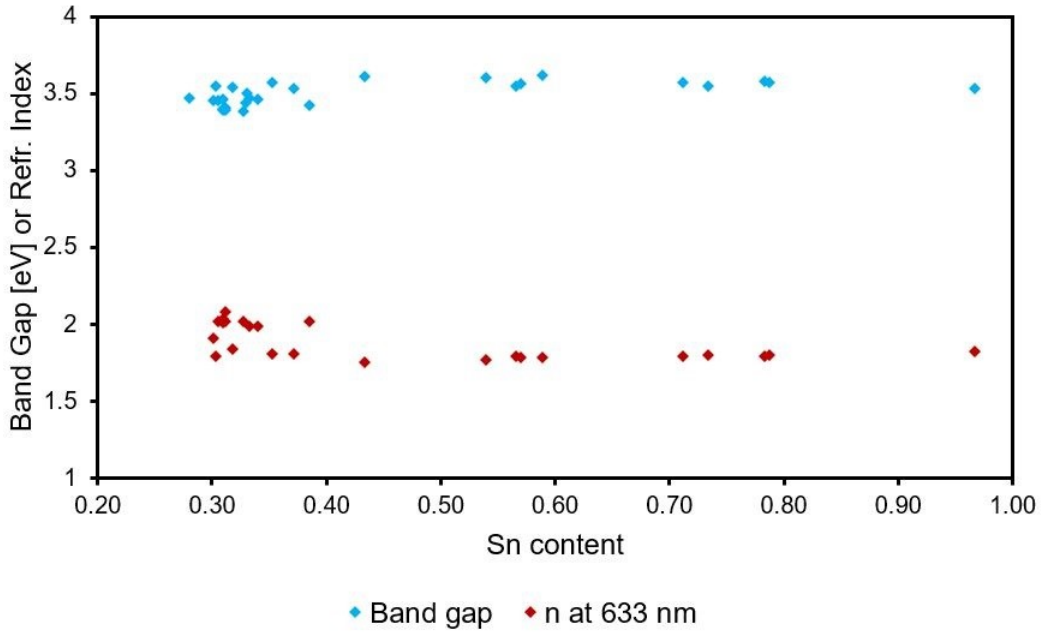

Figure 22: Ellipsometry-obtained E_g & refractive index for ZTO films with thicknesses of 15-310 nm

3.5 Electrical Properties of ZTO

To probe the ITO/ZTO Schottky junction with DLCP, the working electrode was connected to the four Al contacts on the ZTO in turn, and the counter electrode to the ITO's contact. Not every electrode on each film produced usable data, but the X_e against frequency and N against X_e plots obtained generally exhibited the expected curves, with an example shown in Figures 23 and 24 for a film with 71% Sn content that was approximately 200 nm thick. After examination of the literature the dielectric constant of 4 for ZTO was selected for calculations [65,66]. Although the dielectric constant is a function of the frequency and the ZTO composition, the variation remains well within an order of magnitude and so calculation results would not be significantly affected by selection of a different value [65,66]. The chosen value is therefore appropriate for the compositions and frequency range used here.

The value of N at large X_e values tends towards the free carrier density, and at the other end of the X_e range N is the maximum density of states able to respond to the changing AC bias [41]. The difference between these gives an estimate of the defect density of the films, which here was very close to the maximum N value. These results are presented in Table 3. A greater concentration of carriers was seen closer to the junction, and this is not surprising due to the greater concentration of electron-trapping defects that is to be expected near a material interface, due to lattice mismatch among other factors.

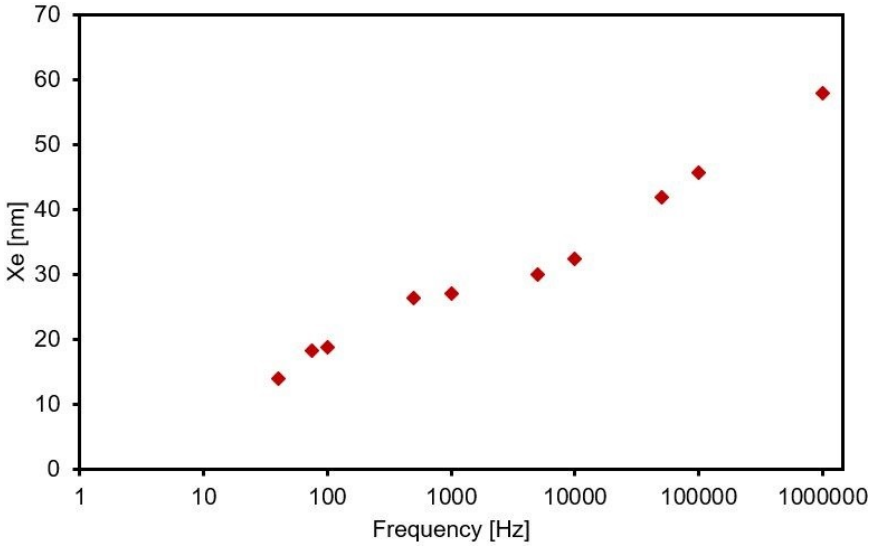

Figure 23: X_e against frequency plot for a ZTO film with 71% Sn content (showing the distance into the film being probed at each frequency)

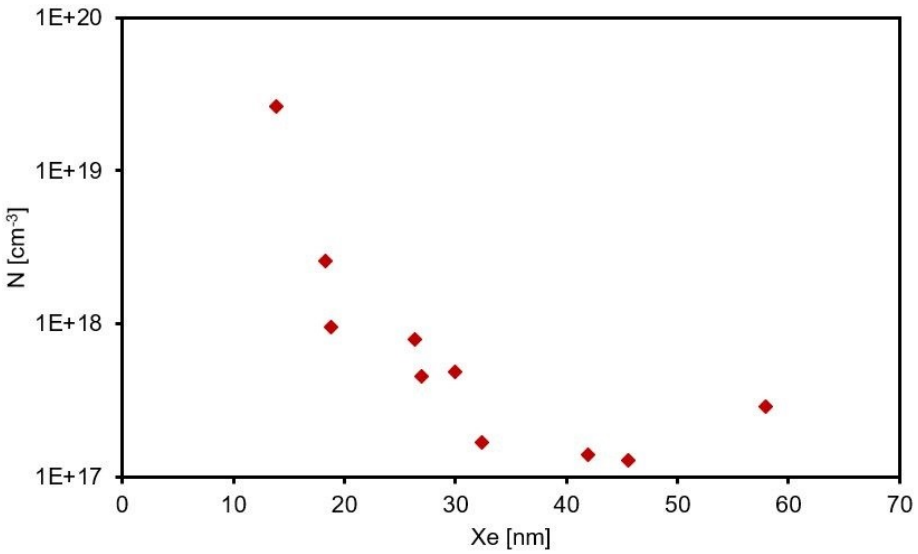

Figure 24: *N* against X_e plot for the same ZTO film with 71% Sn content

Any trend that can be derived from Table 3 may be weak at best. In the last 2 rows the values obtained from plots from two different electrodes on the same film should have been very similar. The fact that they are an order of magnitude apart suggests a lack of precision of the technique (in the way it was carried out here) for the samples used, and implies an uncertainty that may be as high as an order of magnitude for the densities shown. This would invalidate any patterns that could be seen here given that the numbers for one density type are all within one order of magnitude of each other, and we are left to conclude that there is no clear trend in the densities for amorphous ZTO as a function of composition. Although the uncertainty may be as high as one order, it does not mean that the yielded values are inaccurate. The defect densities compare very well to those of SALD-deposited TiO_2 nanofilms measured by DLCP [41], and if the films are all amorphous it would make sense for all of their defect densities to be similar. The carrier concentrations are several orders of magnitude lower than 10^{19}-10^{20} cm^{-3}, or those reported for SALD-deposited ZTO and ZnO films [29]. That said, they compare well to those of sputtered ZTO films [31]. This lower concentration of carriers could be explained in several ways, mostly relating

to the high defect concentration. The defects could occur frequently enough in the amorphous lattice that most of the carriers spend their time trapped in them; they would have a short mean free path. These defects could come from the amorphous nature of the lattice and the accompanying lack of periodicity in its structure, negatively impacting the band overlap between atoms that is preferred for charge carriers to travel in. They could also come from leftover ligands in the film from incomplete reaction as described in section 3.2, or from potential powder inclusions from precursor reacting into a powder on the SALD reactor head and becoming part of the film, as was noticed for a few ZTO films.

Table 3: DLCP-Obtained Carrier and Defect Densities in Films

Film Sn Content [%]	Free Carrier Density [cm^{-3}]	Defect Density [cm^{-3}]
30	$4x10^{17}$	$6x10^{19}$
37	$4x10^{17}$	$8x10^{18}$
71 - electrode 1	$4x10^{16}$	$3x10^{18}$
71 - electrode 2	$3x10^{17}$	$3x10^{19}$

The resistivity of a 277 nm-thick film with 35% Sn content was measured using the van der Pauw 4-point probe technique. Both reciprocal and reversed polarity measurements were performed, but the latter are preferred for films with lower conductivity and only these results will be discussed. The sample resistivity was found to be 1140 Ωcm in ambient lab lighting. As ZnO is photoconductive this measurement was repeated after the sample had been kept in the dark for 12 hours, and interestingly the voltages measured were consistently lower, leading to a resistivity of 847 Ωcm in the dark. ZTO at this composition would therefore exhibit negative photoconductivity, a phenomenon that has been reported before for certain compositions of ZnO-containing oxides [67,68]. Negative photoconductivity is considered an anomaly in materials with n-type

conductivity: in most cases light exposure should boost conductivity through an increase in free charge carrier density [67]. That is if we only consider the material film, and not its environment: support has been found for the claim that the increased conductivity in the dark is thanks to the surface adsorption of water molecules onto the films which are known to boost conductivity. More specifically, it would be the light-induced desorption of water from the material surface that is behind the fall in conductivity once a light is left on [68].

The ZTO film studied here was clearly very resistive, in line with the modest carrier densities obtained by DLCP. The very thin character of the film and the somewhat non-uniform thickness of the sample used here likely did not help with measurement accuracy. It is not the first time that ALD-deposited ZTO nanofilms exhibit very high resistivity [4,30]. However this may change with the amount of Sn content, since in one study in which co-injection SALD of ZTO films was performed, it was found that Sn-doped ZnO (Sn content 0.5%) had the lowest resistivity: 3 mΩcm. When the Sn content was 13% it had risen by three orders of magnitude to 2 Ωcm [29].

If we consider only the majority carriers, then the mobility of the electrons in the ZTO can be estimated using equation (19):

$$\mu = {}^{1}/_{\rho q n} \qquad (19)$$

where p is the film resistivity, q is the elementary charge, n is the majority carrier concentration and μ is the electron mobility in the ZTO. This was carried out for ZTO with ~36% Sn content while taking the resistivity in the light, yielding a value of 0.014 $cm^2/(Vs)$. This value is 1-3 orders of magnitude lower than what was reported for SALD-deposited ZTO films with Sn contents between 0 and 12% [29], and the same number of orders below that reported for sputtered ZTO films with Sn contents of about 50% [31].

3.6 Electron Extraction Capabilities of ZTO

Halide perovskite films were deposited onto the different ETLs to compare their electron extraction efficiencies as a function of composition. PL spectra with the 824-825 nm emission peak of the perovskite [57] are shown in Figure 25. The ETLs of ZTO and ZnO were deposited directly onto glass, the 'glass' sample was a perovskite film directly on glass, and the TiO_2 ETL had 300 nm of ITO between the glass and the ETL, with a final perovskite film on top. This test was repeated twice for the same samples on different days, with somewhat different results in terms of the order of peak heights. The areas of the samples examined was picked randomly each time, so it is probable that different areas of the perovskite films were probed for emission each time, as was the intention for a more representative test. Between the two measurement days the samples were kept in a nearly oxygen-free, moisture-free and dark environment so that degradation of the material between measurements was minimal, and indeed no visible degradation was observed. Figure 25-a and 25-b show the results from the first and second day respectively.

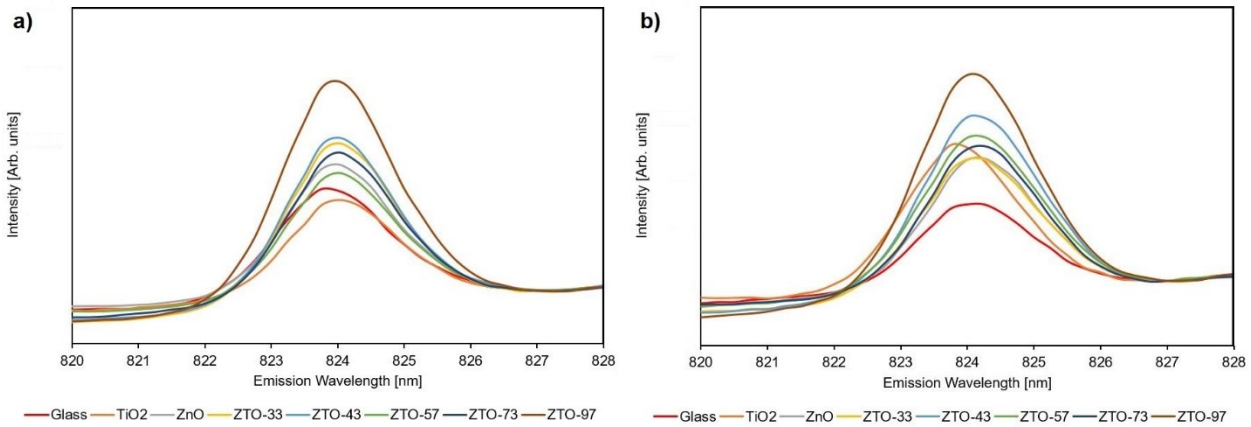

Figure 25: PL quenching for the 824 nm emission peak for perovskite on different ETLs (ZTO-33 means 33% Sn content) on a) day 1 & b) day 2

Table 4 lists the samples in order of lowest to highest PL intensity, where a low PL intensity is expected to correspond to PL quenching resulting from good electron extraction from the

perovskite. The glass result is omitted from the data of the first day, and the TiO_2 data from that of the second day since these peaks were misaligned relative to the rest (e.g. see TiO_2 peak in Figure 25-b), and this difference in emission characteristics was taken as a sign that the perovskite films had formed differently on these underlayers. Thus, the PL intensity could not be directly compared. ETL morphology can greatly affect the quality of a perovskite layer forming on top of it, affecting crystallisation of the absorber layer and the quality of the interface [14]. Not only can different materials exhibit different morphologies, especially if deposited by different methods, but the differences in surface chemistries can impact the quality of the interface and perovskite. Thus, the quenching results presented here may be more useful as a direct comparison between the Zn-containing SALD-deposited ETLs of different compositions to each other, rather than to compare them to glass or a titania ETL. None of the latter were deposited by SALD.

Table 4: ETL Performance (Peak Shallowness) Rankings for Each Test

Rank	Day 1	Day 2
1	TiO_2	Glass
2	ZTO-57%	ZnO & ZTO-33%
3	ZnO	ZTO-73%
4	ZTO-73%	ZTO-57%
5	ZTO-33%	ZTO-43%
6	ZTO-43%	ZTO-97%
7	ZTO-97%	-

Upon examination of the overall performance of only the SALD-deposited ETLs across both days, one inference can be made: the ZTO compositions with 43% and 97% Sn contents consistently seemed to have the least efficient electron extraction capabilities (weakest PL quenching). The 43% ZTO did not have a peak height too different from the next-poorest performer when looking at the data from both days, and so it may be bold to single it out as a poorer performer. But the

peaks for the nearly pure tin oxide cleared the other peaks by quite a wide margin on both occasions, and so there is greater confidence that it was the least effective of the ZTO compositions investigated in this regard. The ranks of the other compositions changed from one day to the next, such that no other conclusions can be made with sufficient confidence about a trend between composition and electron extraction performance. As will be explained when looking at the TCSPC results, the poor quality of the perovskite used, which would have translated into a low degree of photoluminescence, may have been a factor in the quenching tests. An absorber film with low emission could have prevented the full extent of any peak height differences from becoming visible, bunching them closer together and explaining why the rankings across different compositions were not clearer. That said, it is also possible that the Zn-containing ETLs were actually very similar in their electron extraction capabilities. A major factor in electron extraction is the relative level of the CB minimums (CBMs) of the ETL and perovskite. If we look at the indirect bandgaps in Figure 19, some of the lowest E_g values are for the 3 ZTO compositions with the worst quenching on day 1 in Table 4. If the band gap measurements from section 3.4 are to be believed and the ZTO films all had indirect bandgaps of vaguely 3.2 eV, this is significantly lower than that of performant SnO_2 ETLs from literature. Such a mismatch with the CBM of the perovskite could account for somewhat equally poor electron extraction from all ZTO compositions. So could poor interface formation with the perovskite at all compositions, but the results seem to support the theory in claiming that CBM alignment is essential for electron extraction. This further suggests that ZTO films in which the E_g can be tuned, such as in crystalline form or at different composition ranges from those investigated here, could present the desired target ETLs that can perform superbly with a broad range of perovskite absorber layers.

TCSPC measurements were also carried out on the same samples and on the same 2 days as the PL quenching tests, and it is mainly from this test that we suspect that poor perovskite film quality was a factor. This is because all of the curves from each of the samples overlapped, failing to show any discernible difference in the decay characteristics across the different ETLs. The excitation wavelength was 350 nm and emission was measured at 825 nm on one day and 824 nm on the second. Fitting of the decay curves to equation (11) for 1, 2 and 3 lifetimes was carried out. The chi-squared parameter indicating the quality of the fit was not very different across the different number of lifetimes selected, all in the range of 1.13 to 1.3. Increasing the number of lifetimes was mostly akin to simply increasing the number of the same A and τ values, failing to provide different lifetimes which could be attributed to various electron removal processes. Due to this and the curves' overlap, a single decay equation with only one lifetime can be used to represent all of the data from both days quite completely and accurately - with a lifetime of 0.48 nanoseconds. From a comparison to values from past similar studies, the τ value seen here is on the low end of the range observed [7,9,57]. If the lifetime is much shorter than those from literature and the decay curves are not modelled any worse by a single-lifetime equation, it implies a poor-quality perovskite with sufficiently elevated concentrations of recombination centres or electron traps to be a nuisance to explain the lack of variation in the data. The electrons recombining shortly after being raised to the perovskite CB would prevent longer-lifetime processes from being seen, since the charge carriers would not exist long enough to experience them. This PL lifetime test is therefore inconclusive as far as elucidating the effects of the Sn content of the ETLs goes.

3.7 Morphological Characterisation

Some of the ZTO nanofilms were examined by AFM to obtain roughness values and representations of the topography. These are shown in Figures 26 and 27 for ZTO films with Sn contents of 30 and 59% (referred to as ZTO30, 96 nm thick and ZTO59, 47 nm thick), after a first order flattening was applied. From these, average roughness and root mean square (RMS) roughness values were calculated. Two to three AFM images spanning 12 x 12 microns for each film were used to obtain more roughness values, to yield a more representative average of the latter. The different roughness numbers were in close agreement across a given film. The ZTO30 film had an RMS roughness of 1.62 nm and an average roughness of 1.05 nm. The corresponding values for the ZTO59 film were 1.16 nm and 0.60 nm.

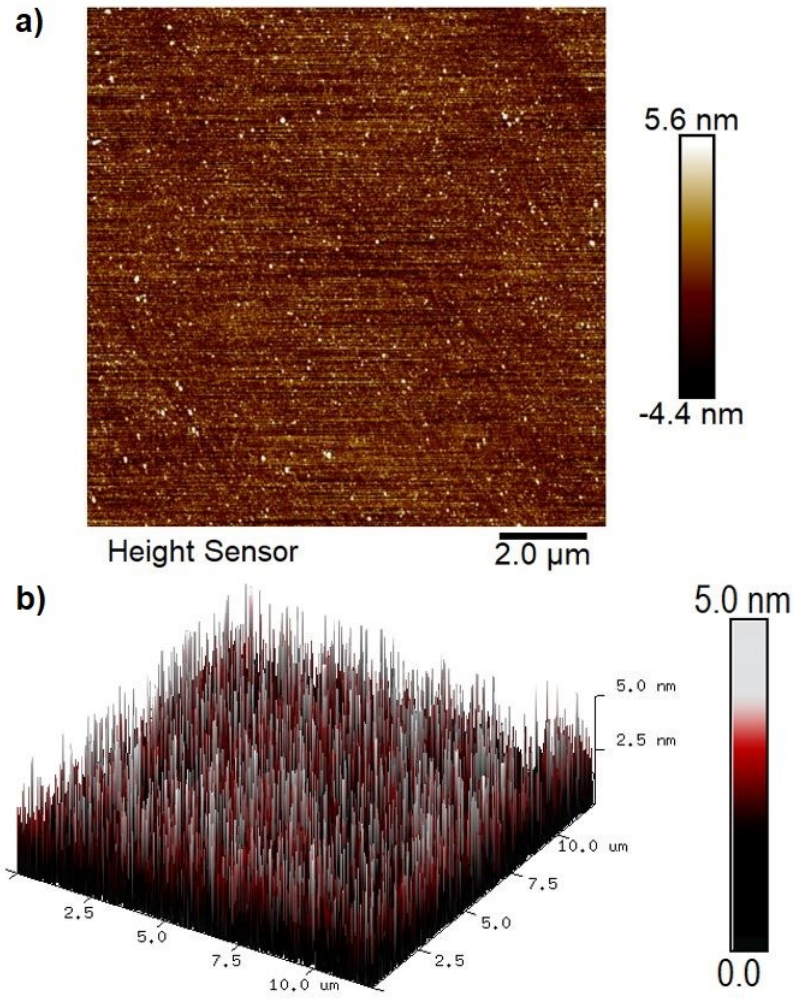

Figure 26: AFM topography renderings from a ZTO film with 30% Sn content: a) 2D image & b) 3D projection for the same area

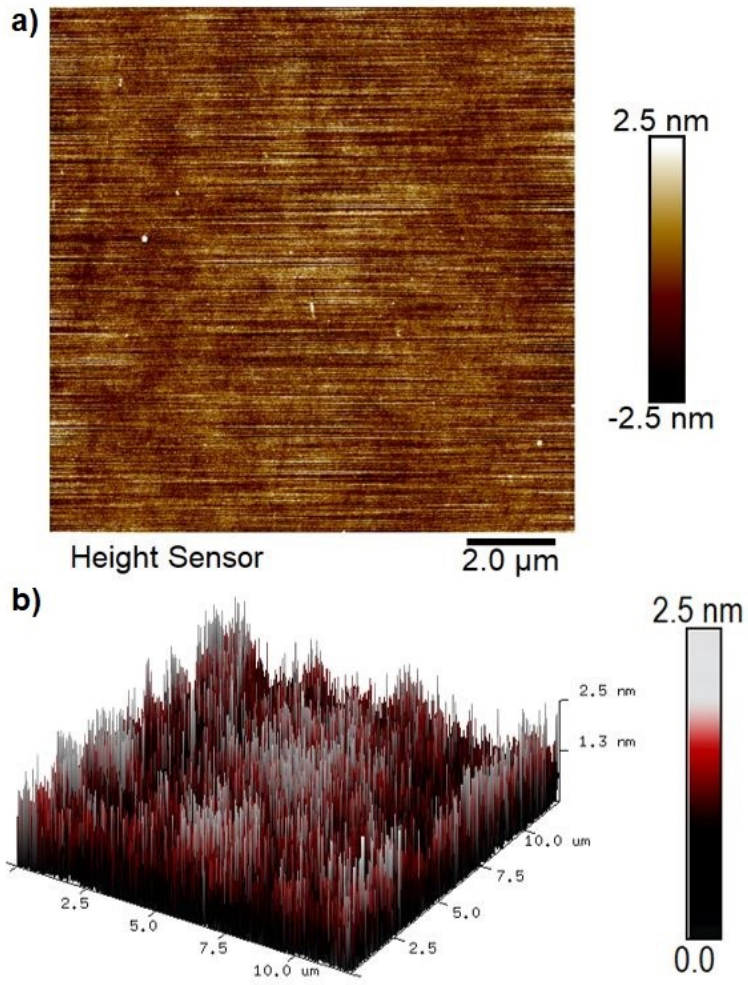

Figure 27: AFM topography renderings from a ZTO film with 59% Sn content: a) 2D image & b) 3D projection for the same area

As expected from depositions with SALD, the films are extremely smooth and flat locally, their somewhat jagged appearance in Figures 26-b and 27-b only being due to the choice of scale. ALD and SALD-deposited SnO_2 nanofilms of comparable thickness grown at similar temperatures have RMS roughness values of about 0.5 nm, so the films examined here compare quite well [32,42], being lower than roughness values for sol-gel-grown metal oxide films [25,69]. The roughness numbers obtained here are what is expected for ALD-grown amorphous metal oxides [32]. This can be seen as a further indication that the ZTO films were amorphous, since higher roughness

values than those observed here are expected for crystalline metal oxide films [41]. No particular features are visible in the 2D or 3D renderings that would indicate grains or grain boundaries. A benefit of such smooth and uniform films for use as ETLs is for the spin-coating of perovskite on top of them [69]. Perovskite deposition atop films such as these should promote the formation of a flat film making smooth contact with the underlying ETL, minimising the formation of voids or other defects which can act as electron traps.

It would be bold to make claims about any relationship between Sn content of the ZTO films and roughness. As will be seen in section 3.8, even 30% Sn content is sufficient to deform the ZnO crystal structure, and so none of the films examined by AFM are expected to be anything but amorphous [5]. Consequently, it is unlikely that amorphous ZTO films with different compositions would exhibit RMS roughness values that are markedly different from the ~1-2 nm ones reported here, at least for the Sn contents studied as part of this project.

Attempts were made to examine many of the ZTO films with SEM, across several different compositions. There was notable difficulty in achieving this: as was just demonstrated by the AFM results, the films were extremely flat, with a lack of 3-dimensional features that aid in focusing and providing contrast for an SEM image, or in yielding interesting images that would allow for comments on microstructure to be made. Figure 28 shows and SEM micrograph for a ZTO film with 57% Sn content, and Figure 29 shows an image of the same film at a higher magnification, which was achieved thanks to the sputtering of a 5-10 nm-thick gold film to aid in preventing surface charging and boost image clarity. The risk is being run that any features visible in Figure 29 are from the gold film rather than the ZTO.

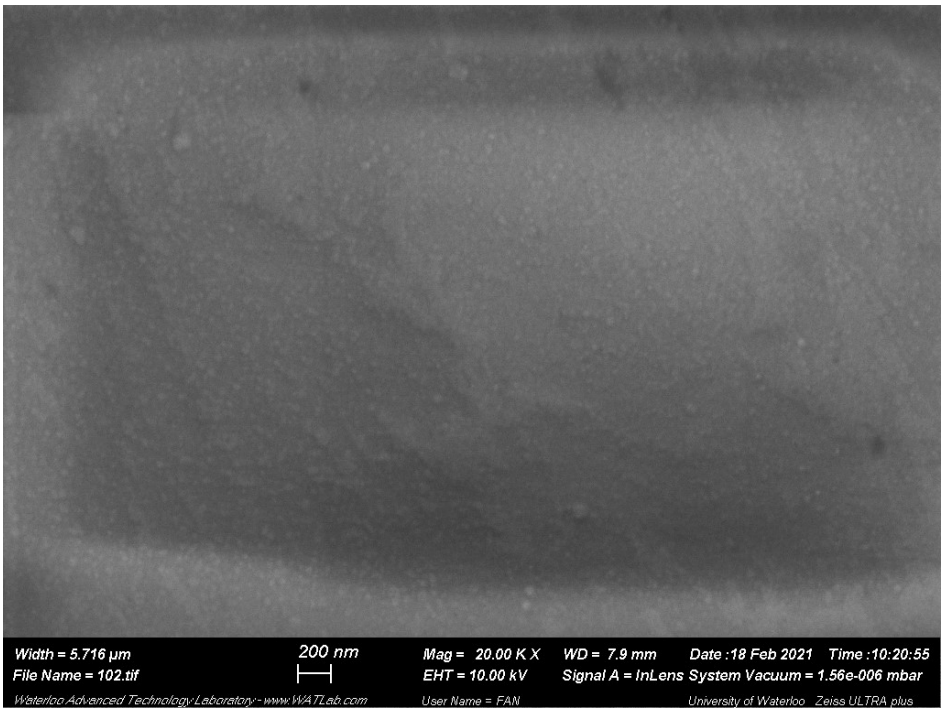

Figure 28: SEM micrograph of a ZTO film with 57% Sn content

The insight that can be gained from the micrographs are a guess that the films are poorly conductive (at least at that composition) and further evidence that the films are extremely smooth with few noteworthy features. Perhaps some features can be seen in Figure 28 in the form of pale specks smaller than 50 nm covering the surface, but given the amorphous character of the films they are not crystals, more likely amorphous agglomerates having to do with the way in which deposition occurred. Although the film surface is still very smooth and flat, a few narrow cracks can be seen in Figure 29, though they may be sputtered gold. ALD-deposited SnO_2 films with comparable thicknesses and deposition temperatures showed similar featureless surfaces, and this was interpreted as a sign of the structure being amorphous [32]. The film with an Sn content of 97% looked closely comparable to Figure 28.

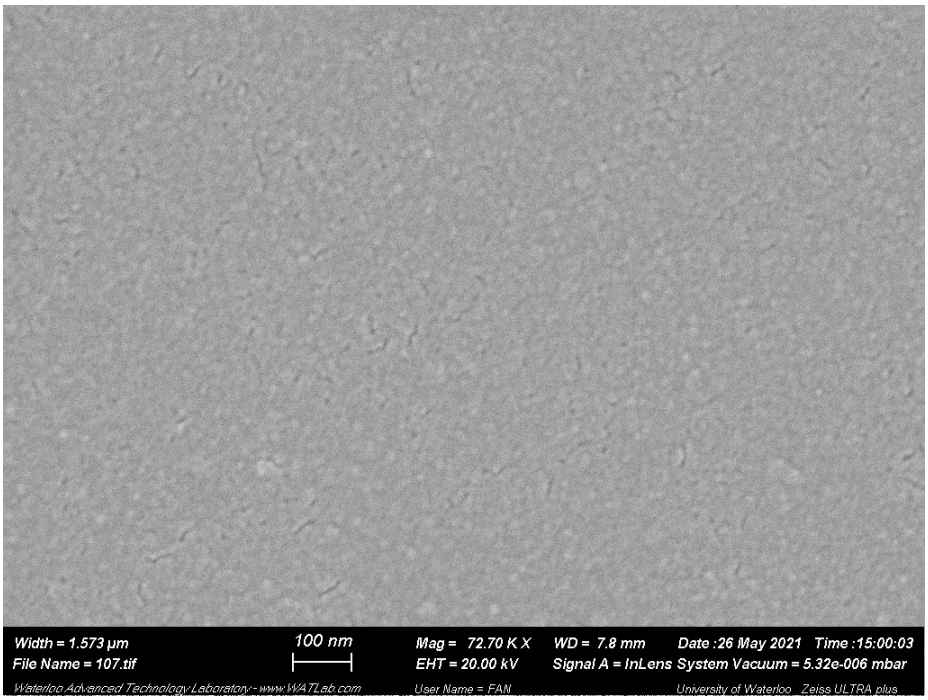

Figure 29: SEM micrograph of the same ZTO film (57% Sn content) with gold sputtering

3.8 Crystallisation of ZTO

ZTO is considered to have two crystalline phases: zinc metastannate ($ZnSnO_3$) and zinc orthostannate (Zn_2SnO_4) [62]. Examination of as-deposited ZTO nanofilms (with Sn contents of approximately 55%) by XRD did not yield any visible peaks that would help to identify the presence of a particular phase. Similar findings have been reported before. In a study of ZTO nanofilm deposition by SALD where deposition took place at 225°C, the films did not exhibit XRD peaks that could signal the presence of any tin-containing phase, be it SnO, SnO_2, $ZnSnO_3$ or Zn_2SnO_4 [29]. Likewise for the case of ALD deposition of ZnO, ZTO and SnO_2 at 120°C. As-deposited ZnO showed the expected XRD peaks, but these faded gradually as the Sn content was increased, and were barely discernible by a content of 34%. This was linked to increased deformation of the ZnO lattice as more Sn was introduced into it, taking the oxide from a

polycrystalline morphology towards something closer to amorphous [5]. Pure ALD-grown SnO_2 films are often amorphous and do not show XRD peaks, even when grown at temperatures as high as 150°C [5,30]. It is therefore not surprising that the XRD scans of ZTO with an Sn content of ~55% from this study resulted in no clear peaks, and evidence points towards all of the ZTO films that were deposited in this project being amorphous.

To investigate this further and induce film crystallisation, annealing of a sample examined by XRD was carried out. Heat treatment of amorphous ZTO nanofilms is expected to bring about the formation of the $ZnSnO_3$ phase at temperatures between 300 and 500°C. Higher temperatures are needed to cause crystallisation of the Zn_2SnO_4 phase [29,62]. The film that was annealed was broken into fragments with different ones heated to 325°C for 15, 30 and 45 minutes in an oxygen-deprived N_2 environment. These nanofilms were then re-examined by XRD and UV-Vis spectroscopy to obtain information on crystallinity and to re-measure their bandgaps and transmittances.

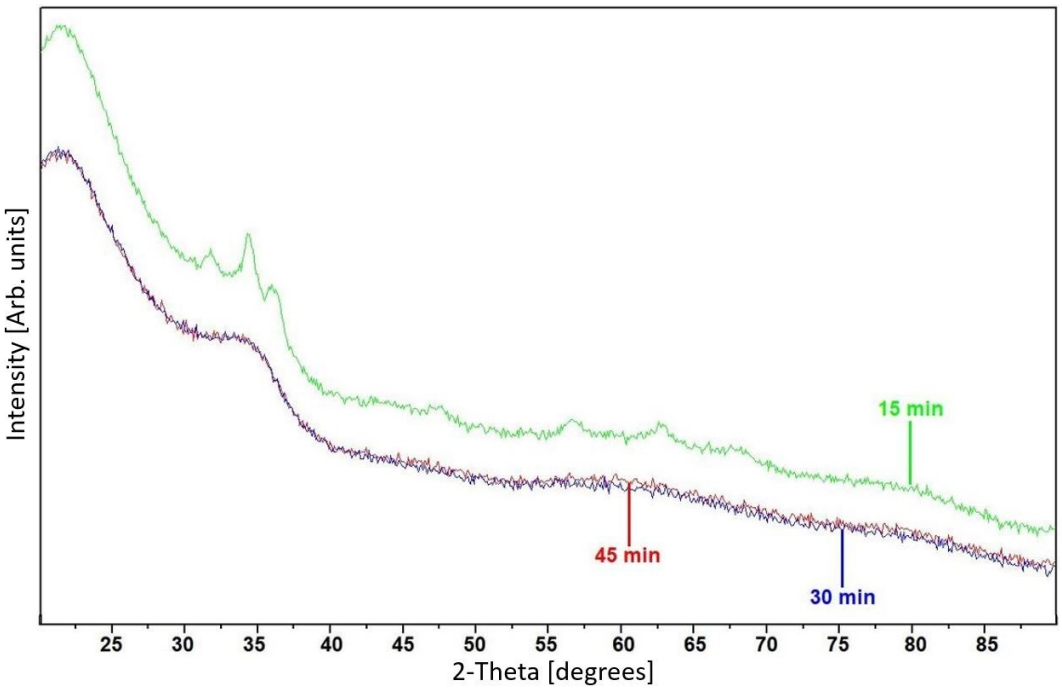

Figure 30: GIXRD spectra for films with 54% Sn content annealed at 325°C for 15, 30 & 45 mins

Surprisingly enough, only one of the 3 samples exhibited any XRD peaks: the one annealed for only 15 min, as shown in Figure 30. It is unclear why no peaks were observed in the samples annealed for 30 and 45 min. The three samples were each a different strip from a 7 x 7 cm glass substrate, which was broken into three strips; one from each of the right, left and centre of the film. Thus, it is possible that there were variations in the film composition and thickness from one end of the film to the other, accounting for the differences in crystallisation behaviour across the samples. The critical information about the observed peaks is summarised in Table 5. All peaks seen most likely correspond to either the ZnO or Zn_2SnO_4 phase, with no peak locations matching those expected for $ZnSnO_3$.

Table 5: Summary of Observed XRD Peaks and Possible Phase Candidates

Approximate 2θ Value [°]	**ZnO Peak (Miller indices of plane)**	**Zn_2SnO_4 Peak (Miller indices of plane)**
32	ZnO (100)	-
34.5	ZnO (002)	Zn_2SnO_4 (311)
36	ZnO (101)	Zn_2SnO_4 (222)
47.5	ZnO (102)	-
57	ZnO (110)	-
62.5	ZnO (103)	-

It is very unlikely that any of the peaks can be attributed to the zinc orthostannate phase. The annealing temperature was not high enough to invite its formation, and if any crystallisation into a documented ZTO phase had taken place, it would have been into zinc metastannate, for which no peaks were seen. Thus, only ZnO peaks were observed. That said, it is certain that crystallisation took place, as seen from the peaks in Figure 30. Figure 31 shows a decrease in the bandgaps following annealing. This decrease in the bandgaps was also seen in the transmittance spectra following heat treatment, but may be challenging to explain. A decrease in bandgap following annealing can occur when the bandgap-widening effects of quantum confinement are reduced upon increases in the crystallite size following annealing. A 9 nm average crystallite size for ZnO is sufficiently small for quantum confinement effects to begin to be seen [4], and ZnO has a direct bandgap of 3.3 eV [29]. Estimating the crystallite size using Scherrer's equation and the most marked peak at 34.5°, an average crystal size of 15.8 nm is found. Thus, the direct bandgap curve in Figure 31 would make sense if the films were pure ZnO, since 15 min of annealing would have grown the crystallites to a size larger than 9 nm, helping the E_g settle to a value close to the bulk value of 3.3 eV. We have seen that amorphous ZTO has an indirect bandgap, and microcrystalline ZTO a direct one [29]. In its nanocrystalline form however, it is unclear which curve of Figure 31

should be focused on. If the bandgap is still indirect, then the values from Figure 31 are very low, and bulk bandgap values are not being approached as the heat treatment time increases: the values are too low for ZTO, ZnO or SnO_2. It is therefore unlikely that the trend in indirect bandgap seen here is attributable to quantum confinement effects. A bandgap of 3.8 eV is expected of crystalline SnO_2, but the amorphous oxide can exhibit an E_g as low as 2.4 eV. This may be due to oxygen atom deficiencies [30]. If the indirect bandgap is relevant for this material, the decreasing values in the lower curve of Figure 31 could be explained by oxygen atom removal from the film following annealing (which was carried out in an O_2-deprived environment). Further testing is in order before more definite conclusions can be made, since overall it is unclear whether the trends seen are from quantum confinement or oxygen removal effects - as it is also unclear which bandgap type best represents the films under consideration.

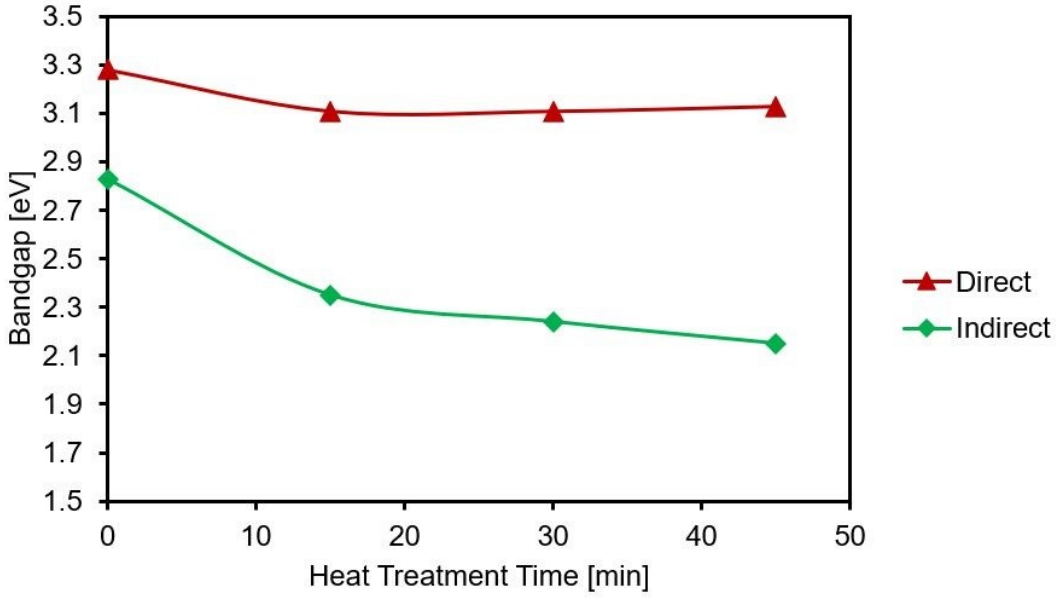

Figure 31: Bandgaps as a function of annealing time for ZTO with 54% Sn content

Crystallisation undoubtedly took place, and yet only ZnO peaks are observed. To reconcile this, it could be that ZnO was crystallising into its usual phases but that its atomic planes were somewhat disrupted by the presence of the Sn atoms trapped in the lattice, preventing the peaks from appearing more distinct. The lack of formation of a recognised ZTO crystal structure raises the question of where the tin atoms lie, and if they are not incorporated into the crystallising ZnO, an alternative explanation could be a sort of phase separation. The zinc oxide, more stable in a tin-free crystal structure at the annealing temperature, would have ejected the Sn from its forming crystals. Whatever atoms were not incorporated into a ZnO crystal lattice would have remained in an amorphous phase between the crystals - a phase that is now more tin-rich.

There was one set of ZTO depositions (Set 3 in Table 1) for which there was a thermocouple malfunction on that day, and the deposition temperature was likely higher than the intended 165°C. It may have been closer to 180 or 200°C. Despite this, E_g determination with Tauc plots did not yield bandgaps that were significantly lower than those of the ZTO grown at the intended temperature, implying a probable lack of any meaningful crystallisation extent even at those higher deposition temperatures, in agreement with the literature [29,62]. Therefore, using temperature for any kind of ZTO bandgap engineering in order to better match it with that of a perovskite absorber layer would very likely involve temperatures well in excess of 200°C to induce crystallisation, either as a deposition or an annealing temperature. If crystallisation is achieved the ZTO would no longer be amorphous, taking us into morphologies where the bandgap is direct. If there is a greater variation in direct ZTO bandgap with composition than in indirect bandgap, this would allow ZTO bandgap engineering thanks to composition control and therefore tailoring of the material to PSC use with a variety of absorber layers.

3.9 Other Results

3.9.1 Investigation into ZTO Film Deposition Directly onto Perovskite

Attempts were made to deposit ZTO and SnO_2 ETLs directly onto perovskite films, an option which may be of use in the manufacturing of PSC stacks, especially for p-i-n solar cell designs. Perovskite can be seen to degrade with the naked eye thanks to a colour change from that of origin to a yellowish hue as the degradation can release lead iodide (PbI_2), one of the reactants often used to synthesise lead perovskites which has a bright yellow-orange colour [3]. After rapid degradation of the perovskite was observed visually through a colour change from dark gray and opaque to yellowish-brown and translucent following depositions with similar conditions to the SALD parameters detailed in section 2.3, an investigation was undertaken to determine the exact cause of this, in the hope of identifying one factor or a combination of them. This is a worthwhile endeavour as DEZ is suspected to react with perovskites, and at temperatures above 110°C the tin precursor TDMASn may remove some of the organic FA^+ cations from perovskites, degrading them [10]. On top of this, the groups who reported these results did not use ozone. The results are detailed in Table 6, in which our SALD apparatus was used to expose perovskite films, made in a similar fashion to that detailed in section 2.4.7, to different combinations of conditions. In row G, unlike for the tests from the other rows of Table 6, no N_2 was made to flow out of the reactor head above the samples at all. The latter could have protected the perovskite from degradation through oxygen displacement, preventing oxidation and therefore identification of potentially harmful deposition parameters to perovskite. The conditions for these tests were a substrate oscillation speed of 3 cm/s, a reactor head height above the substrate of about 0.2 mm, DEZ exposure meant a flow of 50 sccm through the DEZ bubbler and 150 through the carrier line, and these values for water exposure were 150 and 200 sccm respectively. The perovskite films were exposed to the

conditions for 20 min unless degradation was clearly visible prior to that. Exposure to TDMASn was not tested, but it has been reported that SnO_2 deposition on perovskite is less damaging to it than ZnO deposition [10].

Table 6: Degradation of Perovskite Films made to Endure Combinations of Deposition Parameters

Row	Conditions				Outcome
	Temp. [°C]	H_2O	DEZ	Ozone	
A	90		X		No significant degradation after 20 min
B	90			X	Very heavy degradation after 1 min
C	90		X	X	Very heavy degradation after 1 min, unclear if any faster than without DEZ exposure
D	90	X			No visible degradation after 20 min
E	130		X		No visible degradation after 20 min
F	130	X	X		No visible degradation after 20 min
G	165				No visible degradation after 20 min, no N_2 flow this time
H	165	X	X		Possibly some slight degradation after 20 min
I	165			X	Very heavy degradation after 30 secs

The results from this investigation were very clear: ozone ruins the lead halide perovskite as made from the recipe detailed previously at the ozone exposure conditions used to deposit ZTO (280 g/Nm^3). The only tests during which clear degradation was noticed correspond exactly to those where ozone exposure was a factor. When the perovskite was not being exposed to O_3, a combination of parameters that was clearly damaging to the perovskite films was not found, at least from this visual test. However, any deposition where ozone exposure was involved led to clear, rapid damage to the perovskite in only about half a minute. Oxidation is known to be damaging to perovskites, but SCVD depositions have been carried out at high temperatures on them before, including with water and oxygen gas as oxidants, and no damage was recorded as long as the deposition was sufficiently brief. The perovskite is unstable at temperatures above

110°C, but for short deposition processes of about 2 min, SCVD depositions of SnO_2 have been carried out directly onto perovskite with only minimal damage reported at temperatures of up to 180°C [10]. The tests undertaken here are in agreement, with exposure to water and DEZ simultaneously for up to 20 min at relatively high deposition temperatures resulting in minimal damage, if any at all. The tests from rows F and H in which an oxidant and chemical precursor were both present could have led to the deposition of a thin film, although if yes they would have been too thin to notice upon inspection of the sample after the 20 min of deposition. This may have had a protective effect on the perovskite films, shielding them from any effects of prolonged DEZ or water exposure at those higher temperatures that would have led to degradation without this protection. Even if that was the case, the deposition would have achieved the goal of producing a ZnO film without damaging the perovskite, showing that the conditions of those tests seem to still be compatible with deposition on perovskite. That said, not all oxidising agents have the same potency, and from this test it is clear that depositions using ozone are completely incompatible with lead halide perovskite films, unless perhaps very low O_3 flow rates or concentrations are used briefly, or some kind of thin protective film is applied to the perovskite before a deposition using ozone is begun.

3.9.2 Investigation into Potential Antiviral Properties of ZTO

The experimentation undertaken for this project on ZTO was carried out during a period coinciding approximately with the 18 months following the declaration of COVID-19 as a pandemic, which would require the attention of scientists all around the world to help overcome. As such, an investigation was carried out into the potential antiviral effects of the materials our group specialised in depositing, using the human coronavirus 229E as a surrogate for the SARS-CoV-2 virus. The testing was carried out by means of exposing a liquid medium containing a known

concentration of the virus to nanofilm coatings made up of different materials, and measuring the change in virus concentration (viral titers) over time. It was determined that, under the conditions of simple exposure tested, ZTO with an Sn content of about 28% did not show any antiviral effect that would decrease the infectious potential of pathogens left in contact with it, performing very similar to plain glass, zinc oxide and titania [40]. It is possible that these results concerning ZTO would have been different under other testing conditions. For example, ZnO has been observed to have potent antibacterial effects when exposed to UV light [70]. It may be that ZTO coatings would exhibit a similar effect under UV radiation, including for viruses.

Conclusions and Future Work

For some of the tests carried out here, namely the ones involving a perovskite absorber layer and electrical property testing, the test conditions may not have been ideal - due to the poor quality of the perovskite, and non-uniform thickness and/or powder inclusions of the films used in electrical testing. This may have prevented the ZTO films from measuring themselves against established ETLs in literature. The results elucidated here are not sufficient to rule out ZTO as a very performant ETL, but have a use in ruling out certain forms of the oxide that are less useful as ETLs, due to their low conductivity or other features, or certain deposition conditions that do not yield desired forms of ZTO. Consequently, the results of the tests performed here may be more useful to compare different compositions of ZTO in a fair environment than to compare them to TCO materials from other studies - with which a direct comparison would be unfair.

It has been established that SALD can easily deposit ZTO of compositions lying anywhere in the Sn content range of 28 to 97% at the very least. As far as could be told this was the first case of ZTO deposition by SALD using a slit for each precursor rather than by co-injection of precursors, and the composition range achieved by SALD for ZTO here was far broader than ever before. A theory to explain the effects of the deposition parameters on the ZTO composition is detailed, and the results point to this SALD method of ternary metal oxide deposition having potential to control the composition of films with precision and repeatability, at least for ZTO. The parameter combination to be selected to lead to a specific desired Sn content would likely vary across systems (for instance the 21 sccm threshold marking the start of low Zn conditions would not be the same value), but the principle and theory elucidated should remain unchanged.

In the SALD system used here, ZTO was calculated to deposit on average at a rate of 0.07 nm/cycle with 108 cycles needed to nucleate a nascent film onto a glass substrate. The claim that the growth mode was significantly closer to ALD than to CVD was defended. As-deposited films were undoubtedly amorphous, with an indirect bandgap between about 3 and 3.4 eV which does not change very clearly with composition or by more than about 0.4 eV, at least in the broad range studied. Ellipsometry revealed the refractive index at 633 nm to be approximately 1.9, once again irrespective of the composition of the as-deposited films. Nor was a correlation found linking transmittance to composition, with a very high transmittance of 85-95% observed for light energies below the bandgap. At higher energies the transmittance was highly sensitive to nanofilm thickness. The DLCP data was insufficient to determine a trend between defect or carrier densities and composition. Defect densities were 10^{18}-10^{19} cm^{-3} and carrier densities were of 10^{16}-10^{17} cm^{-3} for the films examined. The ZTO films were very resistive and are suspected to demonstrate negative photoconductivity at least at 35% Sn content, but further testing is required to single out any effect from adsorbed water. Higher conductivities may be expected at lower tin fractions. PL quenching singled out ZTO with 97% tin content as too tin-rich with this composition for as-deposited amorphous films having the least efficient ETL performance to extract electrons from perovskite, as determined by PL quenching measurements. AFM inspection judged the films to be extremely smooth, which is encouraging if the formation of a quality, defect-free interface with perovskite is to occur. SEM study confirmed that the nanofilms were smooth and featureless.

Though an important aim was to gain the knowledge necessary to tailor the bandgap of ZTO through composition to allow better synergy with a variety of light absorber materials, this was achieved rather by confirming forms and deposition conditions for ZTO for which this would not work than by directly succeeding in altering the bandgap by larger values, say of ~1 eV. To

summarise, as-deposited amorphous ZTO films with Sn contents between 30 and 97% were found to have indirect bandgaps between 3-3.4 eV which varied more modestly than hoped with composition when deposited within a fixed temperature range. But the crystal structure, type of bandgap, and bandgap variation with composition are expected to be very different at lower Sn contents, as we approach Sn-doped ZnO. Moreover, electrical properties are thought to be superior at low Sn compositions, and thus a bandgap-tunable ETL may be better achieved with tin-poor ZTO compositions. Varying the composition alone in the 30% to 97% Sn content range does not seem an effective strategy to control the bandgap, at least for as-deposited SALD films. For if the films are annealed post-deposition, or if the deposition temperature is varied, then bandgap variation should be seen, as was demonstrated here and in other studies. More noticeable variations in the bandgap with composition may also be seen in films that are partially crystallised following annealing, not to mention higher conductivity through the progressive elimination of electron-trapping defects. This presents a worthwhile opportunity for future research, in which the SALD deposition conditions used here could be used to vary the composition, then annealing the films could allow for a complementary study of the properties of crystalline ZTO as a function of composition. A stronger variation in the properties is expected for crystallised films. 325°C was enough to cause a reduction in the bandgap which was still occurring at 45 min of annealing, and a higher temperature would have produced this effect faster with different crystal structures being formed. After 15 min at 325°C the films had gone from fully amorphous to showing ZnO crystallites with an average diameter of about 16 nm.

Therefore, if these aims of greater conductivity and bandgap tuning can be realised, SALD-deposited ZTO has potential as an ideal ETL material for use with MA^+-free halide perovskites. It would benefit from a near-atomically-smooth surface to favour defect-free interfaces with the

absorber layer to limit recombination, high transmittance, be conductive and rapid to deposit, and should be able to exhibit a bandgap anywhere in the 2.8-4 eV range.

Bibliography

[1] Thambidurai, M.; Shini, F.; Dang, C. Highly stable and efficient planar perovskite solar cells using ternary metal oxide electron transport layers. *J. Power Sources* 448 (2020) 227362.

[2] Kavan, L.; Steier, L.; Gratzel, M. Ultrathin buffer layers of SnO2 by atomic layer deposition: Perfect blocking function and thermal stability. *J. Phys. Chem. C* 121 (2017) 342-350.

[3] Juarez-Perez, E. J. The causes of degradation of perovskite solar cells. *J. Phys. Chem. Lett*. 10 (2019) 5889-5891.

[4] Lindahl, J. Atomic layer deposition of zinc tin oxide buffer layers for Cu(In,Ga)Se2 solar cells. Ph.D. Thesis, Faculty of Science and Technology, Uppsala University, 2015.

[5] Agbenyeke, R. E.; Song, S.; Han, J. Band gap engineering of atomic layer deposited ZnxSn1-xO buffer for efficient Cu(In,Ga)Se2 solar cell. *Prog. Photovolt. Res. Appl*. 26 (2018) 745-751.

[6] Alfakes, B.; Villegas, J.; Chiesa, M. Optoelectronic tunability of Hf-doped ZnO for photovoltaic applications. *J. Phys. Chem. C* 123 (2019) 15258-15266.

[7] Zheng, J.; Deng, X.; Huang, S. Efficient formamidinium-methylammonium lead halide perovskite solar cells using Mg and Er co-modified TiO2 nanorods. *J. Mater. Sci. Mater. Electron*. 30 (2019) 11043-11053.

[8] Cao, T.; Chen, K.; Li, Y. Fullerene derivative-modified SnO2 electron transport layer for highly efficient perovskite solar cells with efficiency over 21%. *ACS Appl. Mater. Interfaces* 11 (2019) 33825-33834.

[9] Lin, L.; Jones, T. W.; Wilson, G. J. Strategically constructed bilayer tin (IV) oxide as electron transport layer boosts performance and reduces hysteresis in perovskite solar cells. *Small* 16 (2019) 1901466.

[10] Raninga, R. D.; Jagt, R. A.; Hoye, R. L. Z. Strong performance enhancement in lead-halide perovskite solar cells through rapid, atmospheric deposition of n-type buffer layer oxides. *Nano Energy* 75 (2020) 104946.

[11] Hoffmann, L.; Brinkmann, K. O.; Riedl, T. Spatial atmospheric pressure atomic layer deposition of tin oxide as an impermeable electron extraction layer for perovskite solar cells with enhanced thermal stability. *ACS Appl. Mater. Interfaces* 10 (2018) 6006-6013.

[12] Zhang, B.; Song, Z.; Song, H. Efficient rare earth co-doped TiO2 electron transport layer for high-performance perovskite solar cells. *J. Colloid Interface Sci*. 553 (2019) 14-21.

[13] Schutt, K.; Nayak, P. K.; Snaith, H. J. Overcoming zinc oxide interface instability with a methylammonium-free perovskite for high-performance solar cells. *Adv. Funct. Mater*. 29 (2019) 1900466.

[14] Zhou, Y.; Li, X.; Lin, H. To be higher and stronger - Metal oxide electron transport materials for perovskite solar cells. *Small* 16 (2019) 1902579.

[15] Wang, J.; Liu, Y.; Duan, Y. Functional metal oxides in perovskite solar cells. *ChemPhysChem*. 20 (2019) 1-8.

[16] Ma, Z.; Zhou, W.; Huang, Y. Negligible hysteresis planar perovskite solar cells using Ga-doped SnO2 nanocrystal as electron transport layers. *Org. Electron*. 71 (2019) 98-105.

[17] Xu, Z.; Teo, S.; Ma, T. La-doped SnO2 as ETL for efficient planar-structure hybrid perovskite solar cells. *Org. Electron*. 73 (2019) 62-68.

[18] Bera, A.; Sheikh, A. D.; Wu, T. Fast crystallization and improved stability of perovskite solar cells with Zn2SnO4 electron transporting layer: Interface matters. *ACS Appl. Mater. Interfaces* 7 (2015) 28404-28411.

[19] Yang, Z.; Zhong, M.; Xu, D. SnO2-C60 pyrrolidine tris-acid (CPTA) as the electron transport layer for highly efficient and stable planar Sn-based perovskite solar cells. *Adv. Funct. Mater*. 29 (2019) 1903621.

[20] Haider, S. Z.; Anwar, H.; Shahid, M. A comparative study of interface engineering with different hole transport materials for high-performance perovskite solar cells. *J. Phys. Chem. Solids* 136 (2020) 109147.

[21] Kim, J.; Chai, S.; Zheng, X. Resolving hysteresis in perovskite solar cells with rapid flame-processed cobalt-doped TiO2. *Adv. Energy Mater*. 8 (2018) 1801717.

[22] Ali, F.; Pham, N.; Tesfamichael, T. Low hysteresis perovskite solar cells using an electron-beam evaporated WO3-x thin film as the electron transport layer. *ACS Appl. Energy Mater*. 2 (2019) 5456-5464.

[23] Pang, Z.; Sun, Y.; Yang, L. Unravelling the mechanism of interface passivation engineering for achieving high-efficient ZnO-based planar perovskite solar cells. *J. Power Sources* 438 (2019) 226957.

[24] Aydin, E.; Allen, T. G.; De Wolf, S. Interplay between temperature and bandgap energies on the outdoor performance of perovskite/silicon tandem solar cells. *Nat. Energy* 5 (2020) 851-859.

[25] Lee, J.; Noh, Y.; Jung, J. Facile surface engineering of nickel oxide thin film for enhanced power conversion efficiency of planar heterojunction perovskite solar cells. *ACS Sustainable Chem. Eng*. 7 (2019) 15495-15503.

[26] Dagar, J.; Castro-Hermosa, S.; Brown, T. M. Low-temperature solution-processed thin SnO2/Al2O3 double electron transport layers toward 20% efficient perovskite solar cells. *IEEE J. Photovolt*. 9 (2019) 1309-1315.

[27] Li, D.; Tong, C.; Han, H. Vanadium oxide post-treatment for enhanced photovoltage of printable perovskite solar cells. *ACS Sustainable Chem. Eng*. 7 (2019) 2619-2625.

[28] Ren, X.; Wang, Z.; Choy, W. C. H. Device physics of the carrier transporting layer in planar perovskite solar cells. *Adv. Optical Mater*. 7 (2019) 1900407.

[29] De Raadt, B. S. P. Spatial ALD of zinc tin oxide: Growth and characterization of zinc tin oxide thin films deposited by co-injection spatial atomic layer deposition. Masters Thesis, Department of Applied Physics, Eindhoven University of Technology, 2015.

[30] Lee, S.; Kim, S.; Min, Y. Band structure of amorphous zinc tin oxide thin films deposited by atomic layer deposition. *J. Ind. Eng. Chem*. 58 (2018) 328-333.

[31] Islam, M. A.; Rahman, K. S.; Amin, N. High mobility and transparent ZTO ETM prepared by RF reactive co-sputtering for perovskite solar cell application. *Results Phys*. 14 (2019) 102518.

[32] Elam, J. W.; Baker, D. A.; Hupp, J. T. Atomic layer deposition of tin oxide films using tetrakis(dimethylamino) tin. *J. Vac. Sci. Technol. A* 26 (2008) 244-252.

[33] Poodt, P.; Cameron, D. C.; Vermeer, A. Spatial atomic layer deposition: A route towards further industrialization of atomic layer deposition. *J. Vac. Sci. Technol. A* 30 (2012) 1-11.

[34] Mackus, A. J. M.; MacIsaac, C.; Bent, S. F. Incomplete elimination of precursor ligands during atomic layer deposition of zinc-oxide, tin-oxide, and zinc-tin-oxide. *J. Chem. Phys*. 146 (2017) 052802.

[35] Muneshwar, T.; Barlage, D.; Cadien, K. Tetraallyltin precursor for plasma enhanced atomic layer deposition of tin oxide: Growth study and material characterization. *J. Vac. Sci. Technol. A* 37 (2019) 030601.

[36] Winarski, D. J. Development of zinc oxide based flexible electronics. Ph.D. Thesis, Bowling Green State University, 2019.

[37] Kuang, Y.; Zardetto, V.; Creatore, M. Low-temperature plasma-assisted atomic-layer-deposited SnO2 as an electron transport layer in planar perovskite solar cells. *ACS Appl. Mater. Interfaces* 10 (2018) 30367-30378.

[38] Tanskanen, J. T.; Hagglund, C.; Bent, S. F. Correlating growth characteristics in atomic layer deposition with precursor molecular structure: The case of zinc tin oxide. *Chem. Mater*. 26 (2014) 2795-2802.

[39] Chistiakova, G.; Mews, M.; Korte, L. In-system photoelectron spectroscopy study of tin oxide layers produced from tetrakis(dimethylamino)tin by plasma enhanced atomic layer deposition. *J. Vac. Sci. Technol. A* 36 (2018) 02D401.

[40] Delumeau, L.-V.; Asgarimoghaddam, H.; Musselman, K. P. Effectiveness of Metal and Metal Oxide Nanofilm Coatings in Decreasing the Infectious Potential of Human Coronavirus 229E. UNPUBLISHED PAPER, being considered for APL Materials (2021).

[41] Armstrong, C.; Delumeau, L.-V.; Musselman, K. P. Tuning the Band Gap and Carrier Concentration of Titania Films Grown by Spatial Atomic Layer Deposition: A Precursor Comparison. UNPUBLISHED PAPER, being considered for Nanoscale Advances (2021).

[42] Hoffmann, L.; Theirich, D.; Riedl, T. Atmospheric pressure plasma enhanced spatial atomic layer deposition of SnOx as conductive gas diffusion barrier. *J. Vac. Sci. Technol. A* 36 (2018) 01A112.

[43] Alshehri, A. H.; Loke, J.; Musselman, K. P. Nanoscale film thickness gradients printed in open air by spatially varying chemical vapor deposition. *Adv. Funct. Mater*. NOT YET IN AN ISSUE (2021) 2103271.

[44] Kim, J.; Jang, Y.; Hwang, C. Substrate-dependent growth behavior of atomic-layer-deposited zinc oxide and zinc tin oxide thin films for thin-film transistor applications. *J. Phys. Chem. C* 124 (2020) 26780-26792.

[45] Ke, C. Investigation of degradation at halide perovskite surfaces using near-ambient pressure X-ray photoelectron spectroscopy. Ph.D. Thesis, Faculty of Science and Engineering, University of Manchester, 2019.

[46] Kersell, H.; Chen, P.; Nemsak, S. Simultaneous ambient pressure X-ray photoelectron spectroscopy and grazing incidence X-ray scattering in gas environments. *Rev. Sci. Instrum*. 92 (2021) 044102.

[47] Aboraia, A. M.; Ezzeldien, M.; Shaaban, E. R. Influence of the indium on the structure and the optical properties of the ZnO thin film: Kramer Kronig relation and the spectroscopic ellipsometry. *Mater. Lett*. 283 (2021) 128783.

[48] Sakulaue, P.; Lertvanithphol, T.; Siriwatwechakul, W. Quantitative relation between thickness and grafting density of temperature-responsive poly(N-isopropylacrylamide-co-acrylamide) thin film using synchrotron-source ATR-FTIR and spectroscopic ellipsometry. *Surf. Interface Anal*. 53 (2021) 268-276.

[49] Wang, Z.; Zhang, R.; Chen, L. The impact of thickness and thermal annealing on refractive index for aluminum oxide thin films deposited by atomic layer deposition. *Nanoscale Res. Lett*. 10 (2015) 46.

[50] Esmaeili, A. Many-body, Pauli blocking and carrier-impurity interaction effects on the band gap of aluminum doped zinc oxide thin films: A new method to evaluate both hole and electron effective masses of degenerate semiconductors. *Curr. Appl. Phys*. 16 (2016) 949-955.

[51] Pan, S. S.; Zhang, Y. X.; Li, L. Optical properties of nitrogen-doped SnO2 films: Effect of the electronegativity on refractive index and band gap. *J. Appl. Phys*. 103 (2008) 093103.

[52] Elisa, M.; Iordache, S.-M.; Enculescu, M. Pulsed laser deposition films based on CdSe-doped zinc aluminophosphate glass. *JOM*. 73 (2021) 495-503.

[53] Dinarelli, S.; Girasole, M.; Longo, G. FC_analysis: a tool for investigating atomic force microscopy maps of force curves. *BMC Bioinformatics* 19 (2018) 258.

[54] Ghobadi, N. Band gap determination using absorption spectrum fitting procedure. *Int. Nano. Lett*. 3 (2013) 2.

[55] Shao, J.; Lu, W.; Chu, J. Modulated photoluminescence spectroscopy with a step-scan Fourier transform infrared spectrometer. *Rev. Sci. Instrum*. 77 (2006) 063104.

[56] Hirvonen, L. M.; Suhling, K. Wide-field TCSPC: Methods and applications. *Meas. Sci. Technol*. 28 (2017) 012003.

[57] Ibrahim, K.; Shahin, A.; Musselman, K. P. Humidity-resistant perovskite solar cells via the incorporation of halogenated graphene particles. *Solar Energy*. 224 (2021) 787-797.

[58] Heath, J. T.; Cohen, J. D.; Shafarman, W. N. Bulk and metastable defects in CuIn1-xGaxSe2 thin films using drive-level capacitance profiling. *J. Appl. Phys*. 95 (2004) 1000-1010.

[59] Unold, T.; Cohen, J. D. Enhancement of light-induced degradation in hydrogenated amorphous silicon due to carbon impurities. *Appl. Phys. Lett*. 58 (1991) 723-725.

[60] Lim, S. H. N.; McKenzie, D. R.; Bilek, M. M. M. Van der Pauw method for measuring resistivity of a plane sample with distant boundaries. *Rev. Sci. Instrum*. 80 (2009) 075109.

[61] Zhen, C. Measurement of resistance of thin film using van der Pauw method. Lecture Slides, Department of Physics and Astronomy, University of Nebraska-Lincoln, 2015.

[62] Mullings, M. N.; Hagglund, C.; Bent, S. F. Thin film characterization of zinc tin oxide deposited by thermal atomic layer deposition. *Thin Solid Films* 556 (2014) 186-194.

[63] Weckman, T.; Laasonen, K. Atomic layer deposition of zinc oxide: diethyl zinc reactions and surface saturation from first-principles. *J. Phys. Chem. C* 120 (2016) 21460-21471.

[64] Lindahl, J.; Hagglund, C.; Torndahl, T. The effect of substrate temperature on atomic layer deposited zinc tin oxide. *Thin Solid Films* 586 (2015) 82-87.

[65] Zankat, A.; Gadani, K.; Pandya, D. D. Frequency and temperature dependent electrical properties of ZnO-SnO2 nanocomposites. *Physica B* 617 (2021) 413140.

[66] Dabbabi, S.; Nasr, T. B.; Kamoun, N. Synthesis and characterization of zinc-tin-mixed oxides thin films. *Superlattices and Microstructures* 123 (2018) 129-137.

[67] Kavasoglu, N.; Kavasoglu, A. S.; Oktik, S. Observation of negative photoconductivity in (ZnO)x(CdO)1-x films. *J. Phys. Chem. Solids* 70 (2009) 521-526.

[68] Peng, L.; Zhai, J.; Xie, T. Anomalous photoconductivity of cobalt-doped zinc oxide nanobelts in air. *Chem. Phys. Lett*. 456 (2008) 231-235.

[69] Lee, J.; Noh, Y.; Jung, J. Efficient perovskite solar cells with negligible hysteresis achieved by sol-gel-driven spinel nickel cobalt oxide thin films as the hole transport layer. *J. Mater. Chem. C* 7 (2019) 7288-7298.

[70] Akhavan, O.; Mehrabian, M.; Azimirad, R. Hydrothermal synthesis of ZnO nanorod arrays for photocatalytic inactivation of bacteria. *J. Phys. D: Appl. Phys*. 42 (2009) 225305.